II.C. SUBTASK 2.c. - SECONDARY REACTION OF PYROLYSIS PRODUCTS AND CHAR BURNOUT SUBMODEL DEVELOPMENT AND EVALUATION

Senior Investigator - Michael A. Serio
Advanced Fuel Research, Inc.
87 Church Street, East Hartford, CT 06108
(203) 528-906

Objective

The objective of this subtask is to develop and evaluate by comparison with laboratory experiments, an integrated and compatible submodel to describe the secondary reactions of volatile pyrolysis products and char burnout during coal conversion processes. Experiments on tar cracking, soot formation, tar/gas reaction, char burnout, sulfur capture, and ignition will be performed during Phase I to allow validation of submodels in Phase II.

Accomplishments

Studies of ignition and soot formation in flames were continued in the transparent wall reactor (TWR) in experiments which include in-situ FT-IR diagnostics. Attention is being focused on what controls ignition (heterogeneous or homogeneous oxidation) and soot formation. Seven additional samples were completed in addition to the four reported in the First Annual Report. Flame properties were compared with characteristics of the samples to determine the factors which control flame behavior. A comparison of the ignition of several samples suggests that the rate of ignition correlates with the initial rate of weight loss in air in a TGA experiment at lower temperatures. Ignition of chars is heterogeneous; ignition of high rank coals is homogeneous; but low rank coals exhibit both homogeneous and heterogeneous contributions to ignition. Soot formation in combustion correlates well with tar yield in pyrolysis suggesting that tar is the chief precursor of soot. Some of the work done under this subtask was discussed in a paper presented at the 22nd Symposium (Int) on Combustion in Seattle, Washington (August, 1988). This paper was included as Appendix A in the Seventh Quarterly Report.

In order to obtain in-situ data from an actual gasifier, an FT-IR spectrometer was temporarily installed at BYU on their high pressure gasifier.

Coal Flame Experiments

Experimental

The experimental apparatus and FT-IR diagnostics were described in the First Annual Report. Figure II.C-1 shows photographs of three flames: a) a lignite which ignites close to the nozzle, b) a low volatile bituminous coal which ignites (apparently homogeneously in the gas phase) higher up, and c) a close up of a high volatile bituminous coal flame showing volatile flames surrounding the particles which are much larger than the particles which they surround.

The samples used in these experiments were sieved fractions of a lignite, a subbituminous coal, and several bituminous coals. Samples have been demineralized by the Bishop and Ward (1958) technique. Chars were prepared from some of the coals in nitrogen in the entrained flow reactor. The characteristics of the coals have been previously published by Serio et al. (1987), Vorres, (1987), and Best et al., (1987). Table II.C-1 summarizes the coals, preparation procedures, and references to the previously published data. The samples were also characterized in a TGA to determine their weight loss at constant heating rate in nitrogen (to

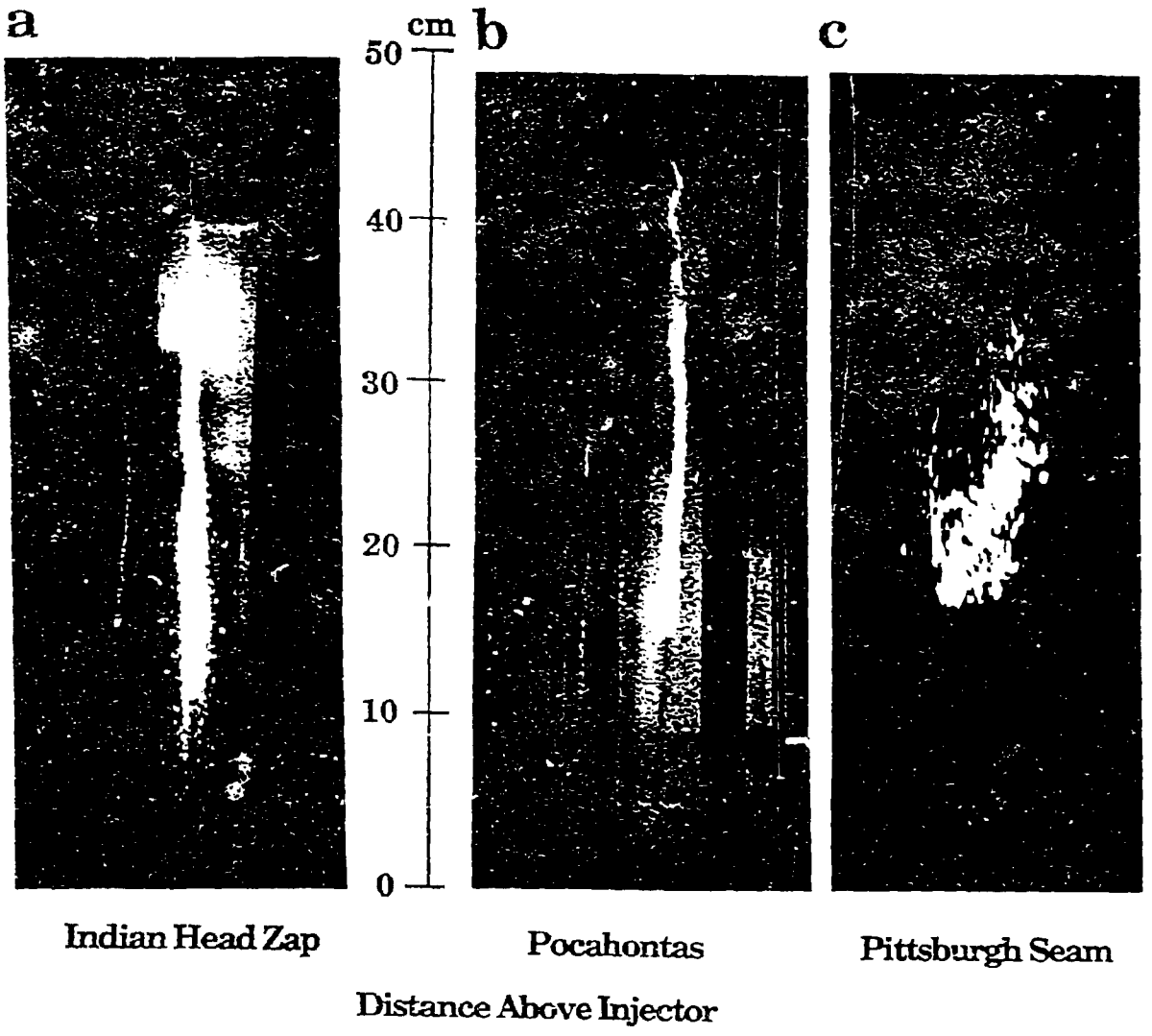

Figure II.C-1. Photographs of a) Zap North Dakota Lignite Flame and b) a Pocahontas Bituminous Coal Flame. The Scale in the Center is Distance Above the Injector Nozzle. c) is a Close up of a Pittsburgh Seam Bituminous Coal Flame.

TABLE II.C-1

SAMPLE CHARACTERISTICS

Sample	Sample Abbreviation in Figures	Classification or Preparation Conditions*	Nominal Particle size (μm)	TGA Analysis				Sample Ref.
				% Ash**	% DAF Volatile*** Matter	T_{cr}(°C)****	$T_{10\%}$ weight loss** (°C)	
Zap	Z	North Dakota Lignite, Dry	45-75	7.3	43.5	434	360	Serio et al. (1987)
Zap 900°C Char	ZC 900	EFR Pyrolysis, 1 m/s 900°C, 66 cm, in N_2	45-75	12.?	22.0	418	388	Serio et al. (1987)
Zap 1500°C Char	ZC 1500	EFR Pyrolysis, 1 m/s 1500°C, 66 cm, in N_2	45-75	14.3	8.8	494	458	Serio et al. (1987)
Argonne Zap	AZ	North Dakota Lignite, Dry	45-75	8.2	40.5	418	335	Vorres (1987)
Zap Demineralized	DZ	HCl, HF washings, Dry	45-75	0.5	44.7	550	383	Solomon et al. (1986)
Rosebud	R	Subbituminous Coal, Dry	45-75	15.1	42.8	485	400	Serio et al. (1987)
Rosebud 900°C Char	RC 900	EFR Pyrolysis, 1 m/s 900°C, 66 cm, in N_2	45-75	23.5	19.1	443	440	Serio et al. (1987)
Rosebud 1500°C Char	RC 1500	EFR Pyrolysis, 1 m/s 1500°C, 66 cm, in N_2	45-75	23.4	2.6	545	575	Serio et al. (1987)
Rosebud Demineralized	DR	HCl, HF washings, Dry	45-75	3.7	39.1	500	432	Solomon et al. (1986)
Argonne Pittsburgh	Pit	Bituminous coal (HVAB)	45-75	3.2	37.2	600	488	Vorres (1987)
Argonne Pocahontas	P	Bituminous coal (LVB)	45-75	5.1	20.0	628	512	Vorres (1987)

* EFR - Entrained Flow Reactor
** TGA analysis in air at 30 K/min to 900°C
*** TGA Analysis in N_2 at 30 K/min to 900°C
**** TGA analysis in N_2 at 30 K/min to 900°C followed by in air at 30 K/min to 900°C; critical temperature defined in (Best et al. (1987 and Solomon et al. (1986)).

determine the volatile content) and in air (to provide a relative measure of the samples' reactivity and the ash concentration).

Results for Seven Flames

Results have been obtained for a series of samples including coal, demineralized coal and char. FT-IR measurements are made along the center of the flame at several positions above the coal injector. It is recognized that the flame is not spatially homogeneous along the line-of-sight. In this case, application of the analysis yields the average properties along a line-of-sight. Work is currently in progress to develop tomographic methods to obtain spatially resolved data. Data on the four Rosebud samples were presented in the Annual Report. Data for the new coals (except the Pocahontas for which insufficient data were obtained due to its unstable ignition very high up in the reactor) are presented in Figs. II.C-2 to II.C-7. The raw data can be found in Tables II.C-2 to II.C-7 in the Seventh Quarterly Report, which also include data on the H_2O concentration (not shown here). The figures present, as a function of distance above the nozzle, the particle and CO_2 temperatures and the black-body multiplier, M, in the upper panel and the soot, CO_2 and particle concentrations in the lower panel. For a completely homogeneous sample of grey-body particles, M would be the particle's emissivity. For the case considered here, some particles may be unignited, or ash particles may be present at a much lower temperature than the coal particles and have a very low emittance. Then, M is approximately the fraction of particles ignited times their emissivity.

A Correlation of Flame Properties with Sample Characteristics

Several flame characteristics which varied with sample properties were examined to determine what sample properties were the controlling factors and why. A comparison of the CO_2 concentration profiles, which is a by-product of the ignition behavior, is presented in Fig. II.C-8a, for the raw and demineralized Rosebud coal, and Rosebud chars produced at 900°C and 1500°C. Ignition for the coals is accompanied by a more rapid increase in CO_2 than seen for the chars. This is believed to be due to the rapid release of energy from the combustion of volatiles. The position of the ignition also varies for the four samples.

To determine what controls the ignition, measurements have been made of the weight loss of coal in a TGA, both under inert and oxidizing conditions. The objective is to correlate what happens in the TGA at temperatures from 450°C to 600°C to what happens during ignition in the TWR at similar particle temperatures. As shown in Fig. II.C-8b, the ignition distance correlates well with the temperature for 10% weight loss in air measured at a constant heating rate of 30°C/min in a TGA. The lower the temperature to achieve 10% weight loss in the TGA, the shorter the ignition distance in the TWR.

In the case of the previously formed chars, the TGA weight loss is almost exclusively due to char oxidation and hence, the ignition in the TWR must be heterogeneous (i.e., within the porous solid matrix). For high rank coals, the first 10% weight loss in the TGA under oxidizing conditions is mostly due to pyrolysis, consistent with homogeneous ignition in the TWR. For low rank coals, however, there is a significant early weight loss in the TGA due to heterogeneous oxidation, and it appears that there is a significant heterogeneous contribution to the ignition in the TWR. This is consistent with the observation that the demineralized Rosebud coal (which is less reactive to oxidation than the raw coal) is more difficult to ignite (Fig. II.C-8a). The results are also consistent with the measurements of Midkiff et al. (1986) who conclude that there is a significant weight loss due to heterogeneous oxidation in combustion for low rank coals.

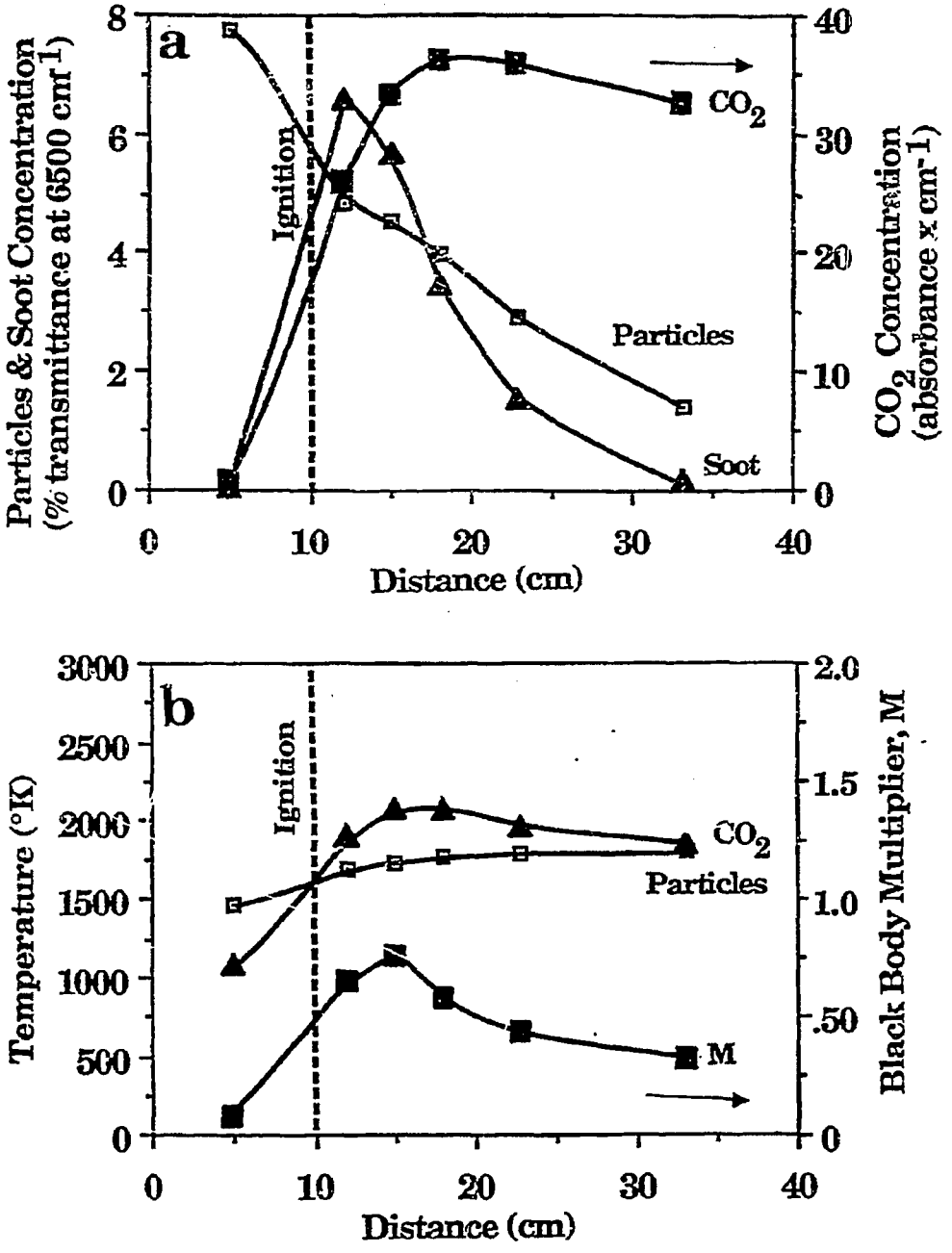

Figure II.C-2. Flame Properties as a Function of Distance Above the Injection Nozzle for Zap North Dakota Lignite. a) Concentrations of CO_2, Particles and Soot and b) Temperature of Particles and CO_2 and Percent of Particle Ignited Times Emissivity.

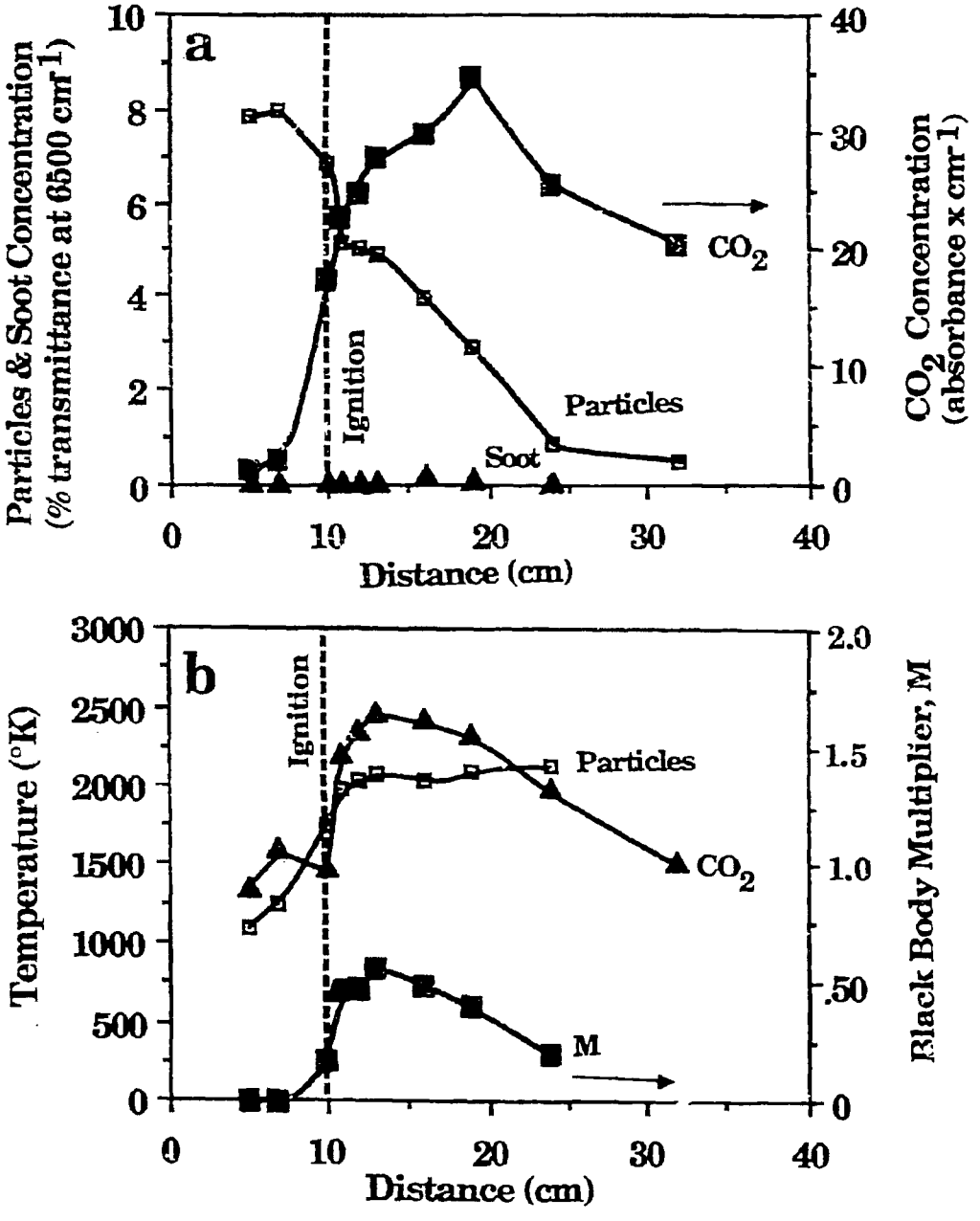

Figure II.C-3. Flame Properties as a Function of Distance Above the Injection Nozzle for Zap North Dakota Lignite 900°C Char. a) Concentrations of CO_2, Particles and Soot and b) Temperature of Particles and CO_2 and Percent of Particles Ignited Times Emissivity.

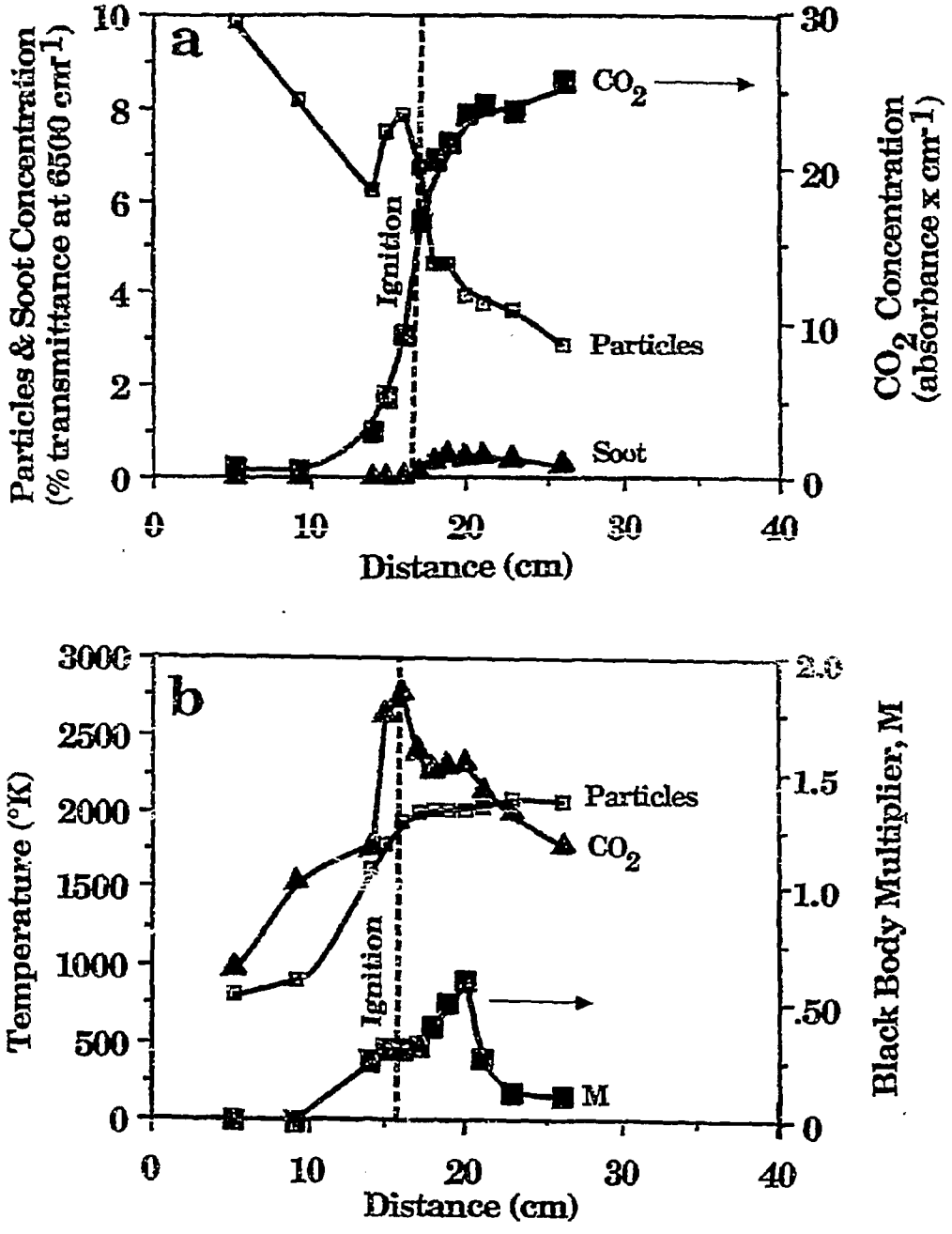

Figure II.C-4. Flame Properties as a Function of Distance Above the Injection Nozzle for Zap North Dakota Lignite 1500°C Char. a) Concentrations of CO_2, Particles and Soot and b) Temperature of Particles and CO_2 and Percent Particles Ignited Times Emissivity.

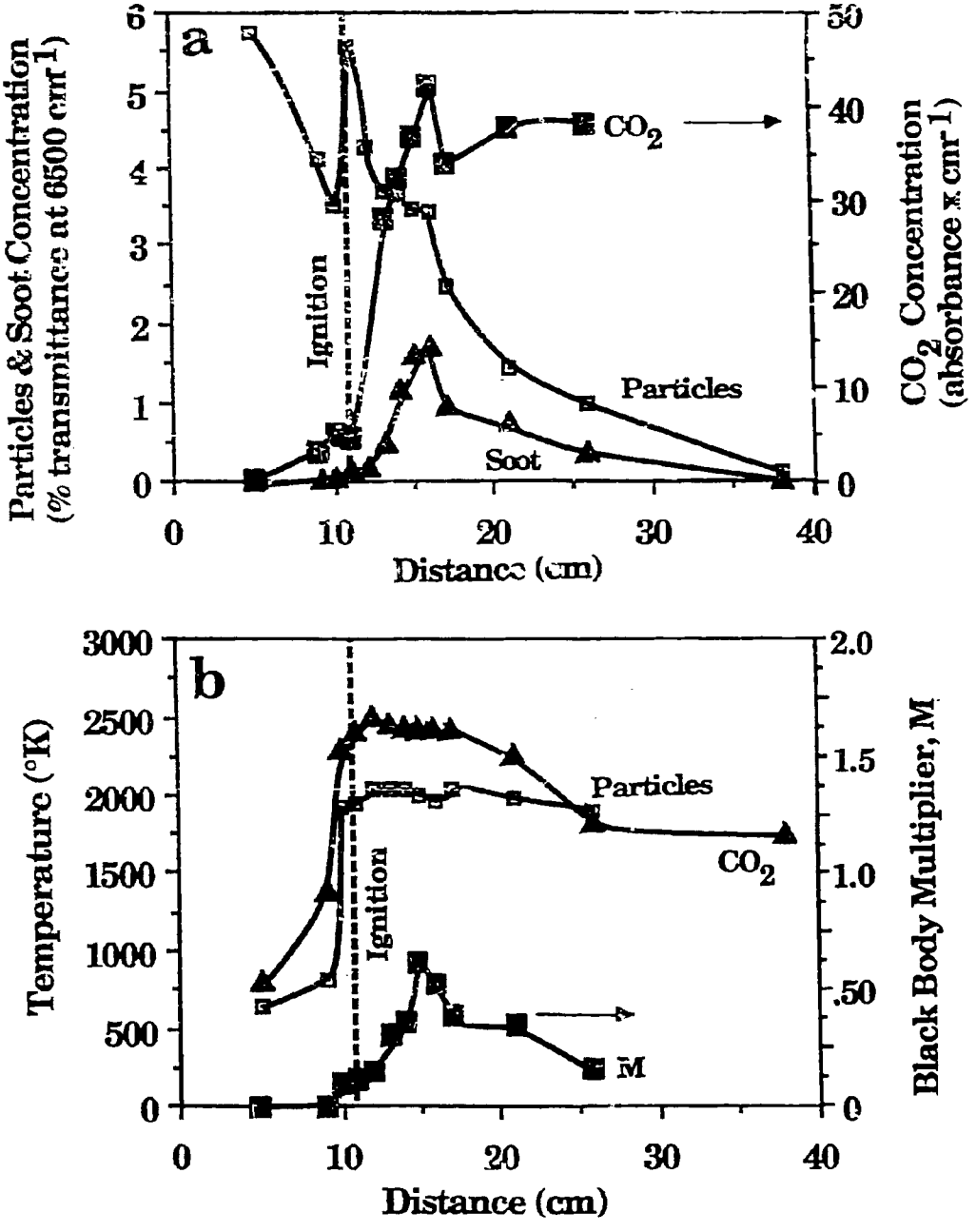

Figure II.C-5. Flame Properties as a Function of Distance Above the Injection Nozzle for Argonne Zap North Dakota Lignite. a) Concentrations of CO_2, Particles and Soot and b) Temperature of Particles and CO_2 and Percent of Particles Ignited Times Emissivity.

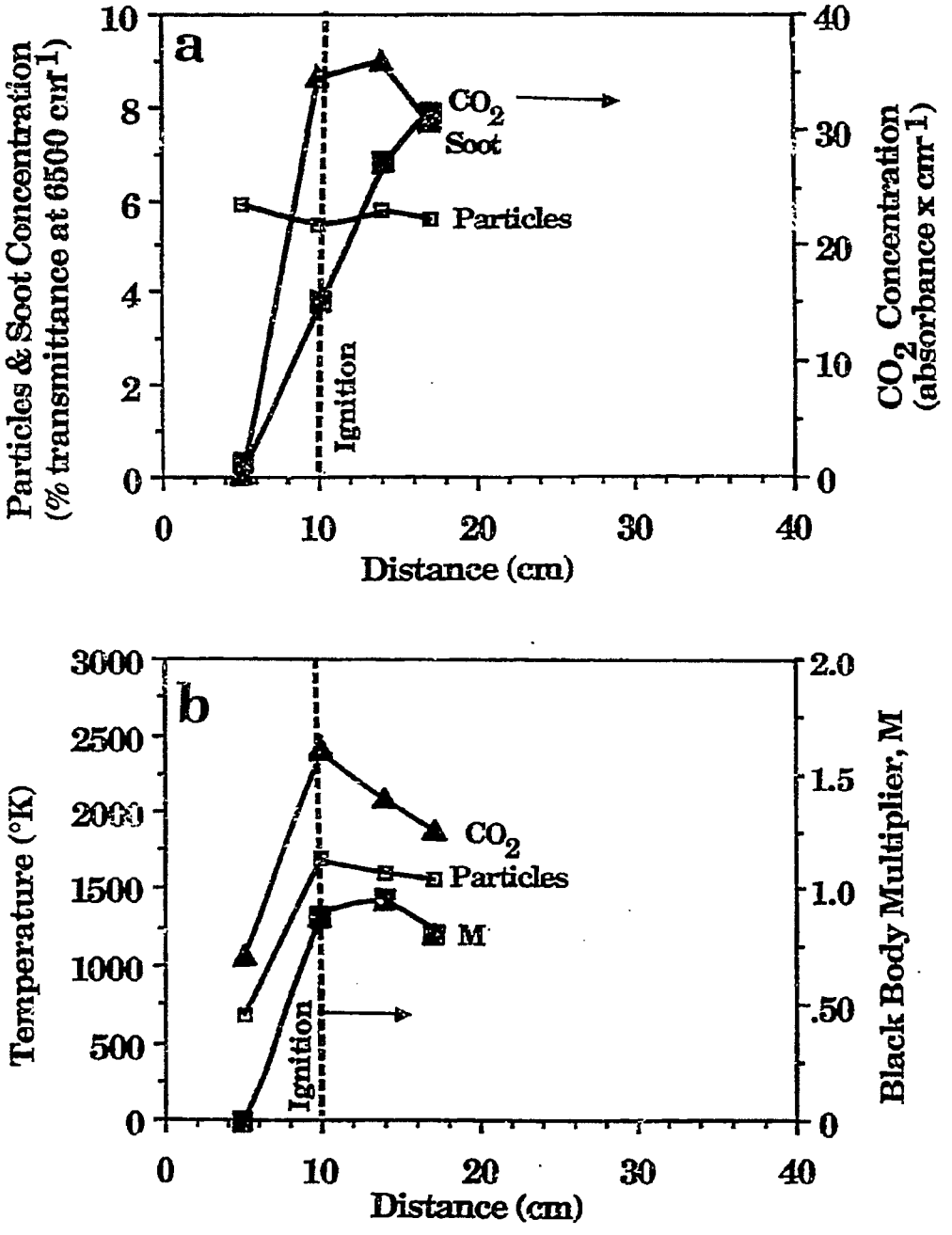

Figure II.C-6. Flame Properties as a Function of Distance Above the Injection Nozzle for Demineralized Zap North Dakota Lignite. a) Concentrations of CO_2, Particles and Soot and b) Temperature of Particles and CO_2 and Percent of Particles Ignited Times Emissivity.

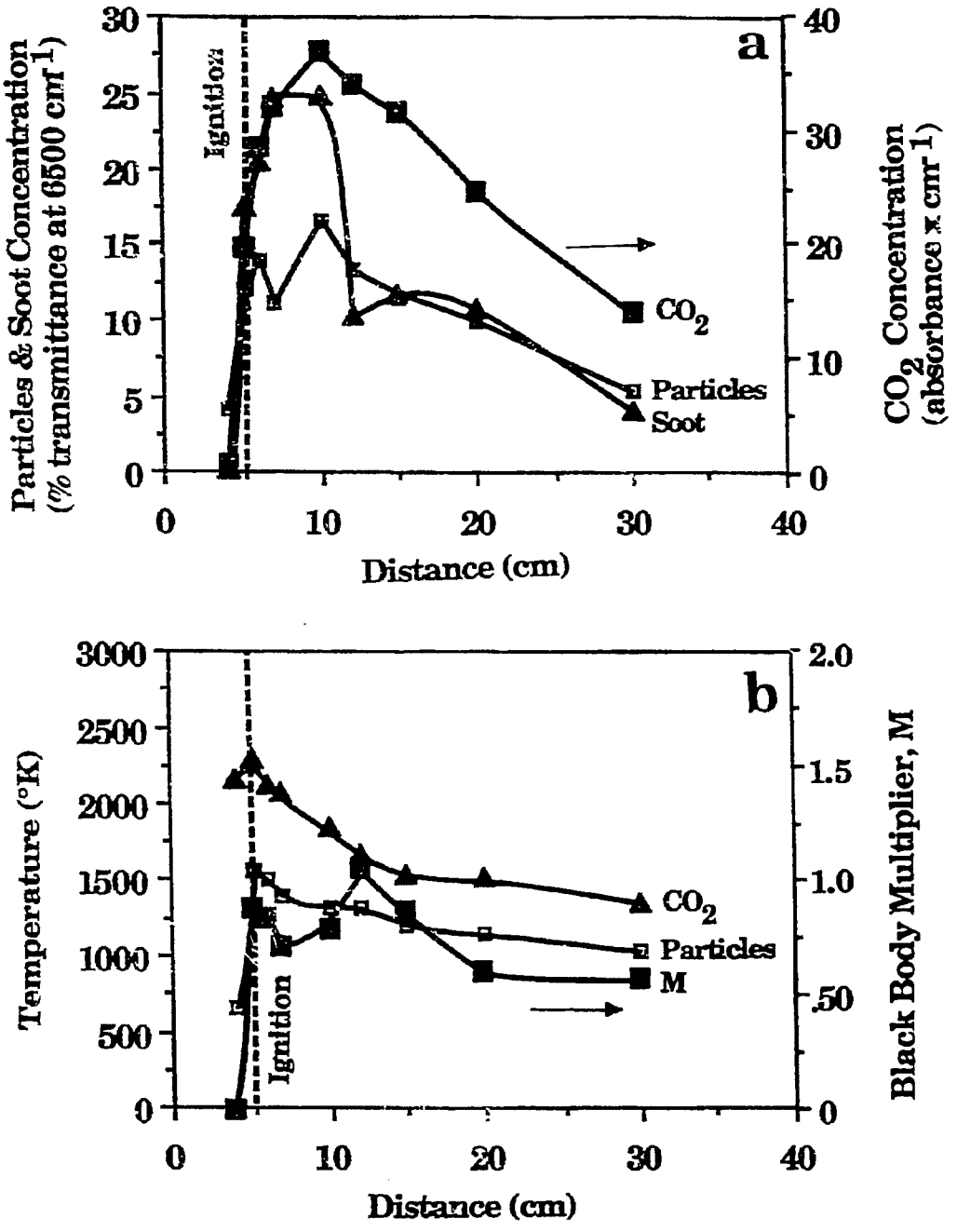

Figure ILC-7. Flame Properties as a Function of Distance Above the Injection Nozzle for Argonne Pittsburgh Seam Bituminous Coal. a) Concentrations of CO_2, Particles and Soot and b) Temperature of Particles and CO_2 and Percent of Particles Ignited Times Emissivity.

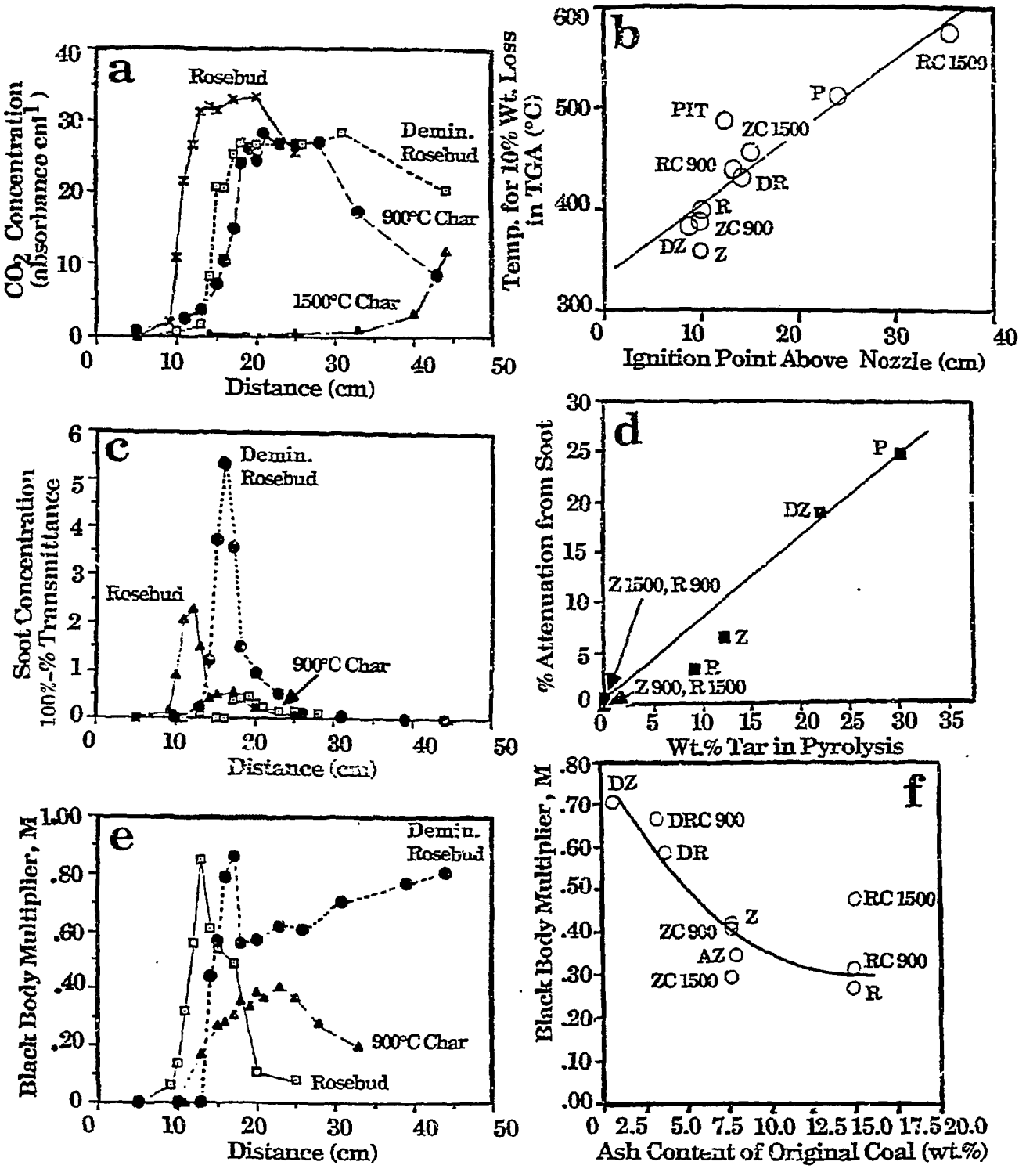

Figure II.C-8. Selected Flame Measurements and Correlation of Flame Measurements with Coal Properties. a) Comparison of CO_2 Concentration in Flames of Four Samples, b) Correlation of Ignited Point with TGA Weight Loss in Air, c) Comparison of Soot Yields for Three Samples, d) Correlation of Soot Yield with Tar Yield in Pyrolysis, e) Comparison of Black Body Multiplier for Three Samples, and f) Correlation of Black Body Multiplier with Ash Content of the Coal.

A comparison of the soot concentration for 3 samples is shown in Fig. II.C-8c. The demineralized Rosebud produces about twice the soot as the raw sample, and the char produces almost none. As shown in Fig. II.C-8d, the soot production correlates well with the yield of tar as determined in pyrolysis experiments. Pyrolysis was performed in the entrained flow reactor. The higher the tar yield, the higher the soot yield. The relationship between tar and soot is consistent with the results of Wornat et al. (1981) and Nenniger et al. (1983).

Figure II.C-8e compares M for the raw coal, the demineralized coal and the 900°C char. M can be less than 1.0 due to unignited particles and/or a low value of emissivity. Prior to ignition, all three samples have low values of M due to unignited particles. At ignition, M for the two coals goes up rapidly as the particles ignite and soot is formed. Above the ignition region, where all the particles are expected to be ignited, M drops rapidly for the raw coal but remains high for the demineralized coal. The source for this effect appears to be ash particles which are on the surface or are shed from the burning char particles. The ash particles that are shed will increase (100%-transmittance) without adding significantly to the radiance because of their low temperature and low emissivity. TGA analysis of the captured samples of char showed that a significant fraction of the minerals (30%) had already been shed. An alternative explanation is that the unshed ash particles act as diffuse scatterers which lowers the emissivity. However, a direct measurement of the emissivity of captured char particles using the E/T technique at a lower temperature (800°C), shows that the emissivity to be approximately 0.85, suggesting that the reduction of the emissivity due to surface ash is not important.

Figure II.C-8f presents a correlation between M above ignition (where all particles should be ignited and the soot has been consumed) with the ash content of the coal. The higher the ash content, the lower M, in agreement with either hypotheses.

Conclusions from Coal Flame Experiments

The FT-IR E/T technique is a versatile technique for coal combustion diagnostics allowing measurements of particle concentrations and temperatures and gas compositions, concentrations, and temperatures.

A comparison of the ignition of several samples suggests that the rate of ignition correlates with the initial rate of weight loss in air in a TGA experiment at lower temperatures. Ignition of chars is heterogeneous; ignition of high rank coals is homogeneous; but low rank coals exhibit both homogeneous and heterogeneous contributions to ignition.

Soot formation in combustion correlates well with tar yield in pyrolysis suggesting that tar is the chief precursor of soot.

In-Situ Diagnostics in a Gasifier at Brigham Young University

In order to provide in-situ data on several gasification cases, measurements were made in the BYU gasifier using the FT-IR E/T method. The gasification tests were being performed under Subtask 2.h. A Michelson M-110 spectrometer modified for E/T was used to collect data. The instrument was modified to make E/T spectral measurements through a side port. Also, purge fittings were installed and the source was turned up to 1200°C.

The instrument and components were packed in 5 boxes at AFR and shipped to Utah as airline luggage. No tuning of the instrument was required when it arrived at BYU. The arrangement of the diagnostics and gasifier is illustrated in

Fig. II.C-9. The Michelson 110 was suspended from the ceiling of the room with the gasifier and lined up to aim through optical ports of the gasifier. The optical ports are in the second section of the gasifier where the coal has just started oxidizing. Silicon windows were employed on the gasifier. The transmission detector (MCT) was suspended from the ceiling on the opposite side of the gasifier. The emission detector (MCT) was mounted near the Michelson 110. The distance across the reactor was about 25 cm. About a day was necessary for set up, and another day for getting acquainted with idiosyncracies of the system. The conditions in the room were ~ 50°C on the average, and some water cooled plastic tubes draped over the instrument helped to cool it.

Data were collected on two coals (Alberta and Utah) run at various O_2/coal ratios (1.0 - 0.5 mass ratio). These runs were taken at one height in the flame, as a function of oxygen feed rate for a constant coal feed rate. Adequate signal averaging for the M-110 infrared range was accomplished by four minutes for transmission and 2 minutes for emission. The data will be presented and discussed in the Ninth Quarterly Report.

Plans

Continue the TWR flame experiments for the remaining standard samples. Analyze the results of the in-situ FT-IR diagnostic measurements on the BYU gasifier.

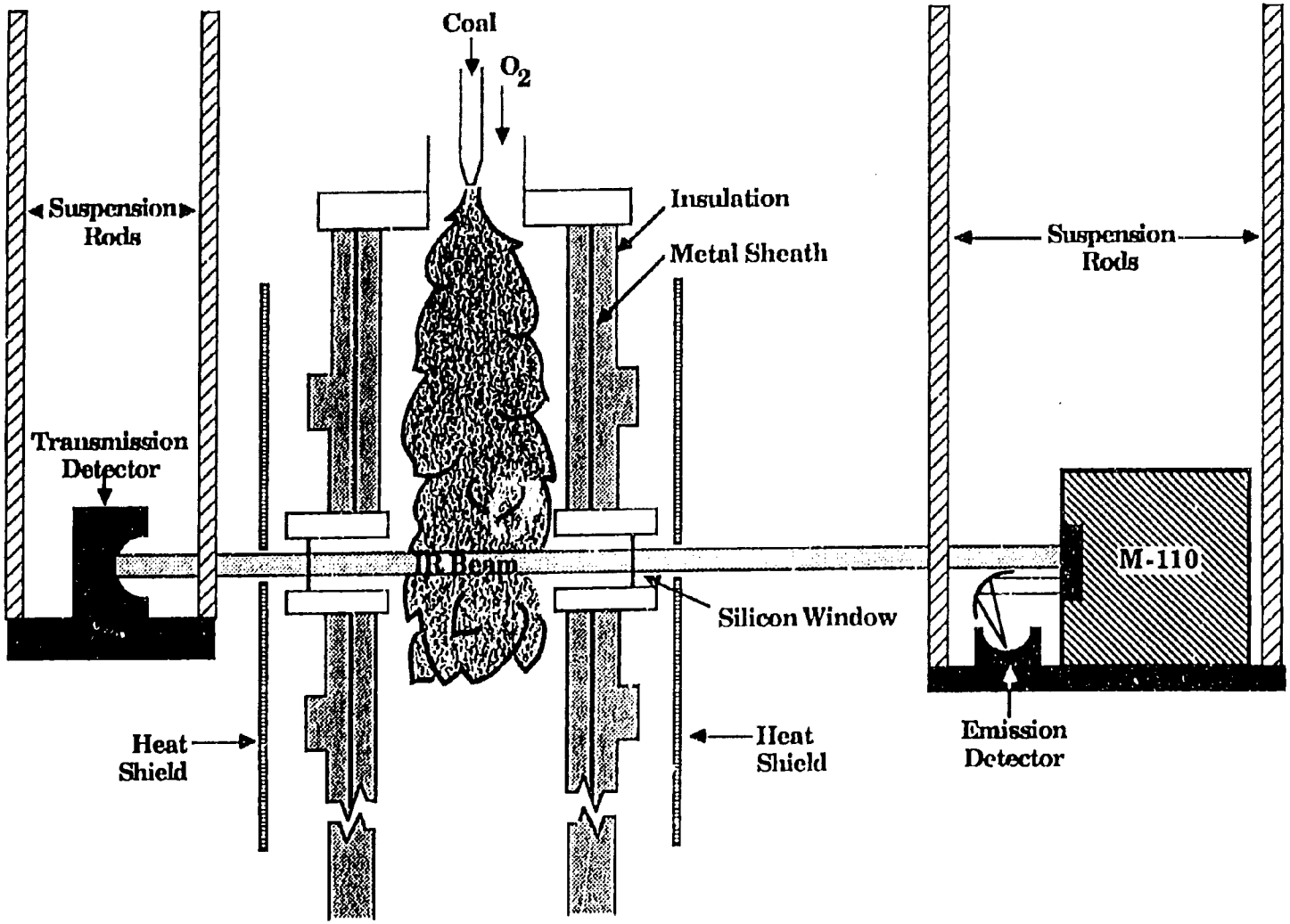

Figure II.C-9. Schematic of BYU Gasifier with In-Situ FT-IR Diagnostics.

II.D. SUBTASK 2.d - ASH PHYSICS AND CHEMISTRY SUBMODEL

Senior Investigator - James Markham
Advanced Fuel Research, Inc.
87 Church Street, East Hartford, CT 06108
(203) 528-906

Objective

The objective of this task is to develop and validate, by comparison with laboratory experiments, an integrated and compatible submodel to describe the ash physics and chemistry during coal conversion processes. AFR will provide the submodel to BYU together with assistance for its implementation into the BYU PCGC-2 comprehensive code.

To accomplish the overall objective, the following specific objectives are: 1) to develop an understanding of the mineral matter phase transformation during ashing and slagging in coal conversion; 2) To investigate the catalytic effect of mineral matter on coal conversion processes. Emphasis during Phase I will be on the acquisition of data which will be utilized for model development in Phase II. Data acquisition will be focused on: 1) design and implementation of an ash sample collection system; 2) developing methods for mineral characterization in ash particles; 3) developing methods for studying the catalytic effect of minerals on coal gasification.

Mineral matter in coal is a source for slagging and deposits on reactor or down stream component walls, causing corrosion of equipment. Minerals can also catalyze reactions or can poison processing catalysts. The objective of this research is for the development of a model for the prediction of ash behavior and the correlation of the behavior with the original chemical composition, particle size, physical properties of the minerals and the process conditions. A model will also be developed to predict the catalytic effect of minerals on coal conversion.

Accomplishments

During the second year, two sample collection probes were constructed that can be inserted into the transparent wall reactor (TWR) to allow for the collection of char with its transforming mineral matter from the flame at various stages of burnoff, and of fly ash from above the flame. Both probes result in no visual disruption of the stability, size or ignition delay time of the flames. Sample collections were performed using these probes from Zap lignite and Montana Rosebud coal flame experiments. SEM/dispersive x-ray analysis was performed on individual ash spheres that were recovered from the preseparator and the eight stages of the cascade impactor for an "in stack" ash collection from 200 x 325 mesh Zap lignite.

In order to further understand the role played by ion-exchanged cations on char reactivity, samples of demineralized Zap coal were subjected to ion-exchange experiments with Ca, Na, Mg, and K. The reactivity of the resultant chars was measured in air and CO_2.

Ash Collection

The fly ash collector (in stack) consists of an inlet nozzle, large particle preseparator, cascade impactor and adjustable air pump. The char collector (in flame) consists of a water cooled nozzle that adds cold helium gas to the removed hot particle stream. After quenching, the particle stream passes through a large

particle cyclone separator, and then through the preseparator and cascade impactor. A schematic of the system, as installed in the transparent wall reactor (TWR) is shown in Fig. II.D-1.

The char collector nozzle inlet temperature was maintained below 300°C by the He addition. The fly ash collector nozzle was placed in the flame exhaust stack having a typical radial temperature profile as presented in Fig. II.D-2.

Table II.D-1 and Fig. II.D-3 show collection and separation data for a Rosebud subbituminous coal and a Zap lignite under similar collection conditions. TGA weight loss measurements on the in-flame collected samples indicate that both cyclone fractions have a large amount of burnable material remaining (~60%). SEM photomicrographs (Figs. II.D-4 and II.D-5) show both materials to contain etched particles of the same size range of the starting materials, with some particles having discrete globules of ash stuck to the particle surface and others with a more uniform coating (possibly smaller globules) of ash as indicated by the bright (charging) areas. The Zap cyclone fraction appears to contain more particles with ash globules on particle surfaces and more ash that has apparently released from the char. This is also indicated in the size separation data presented in Fig. II.D-3. For the Zap sample, there is more material collected downstream of the large particle separators than for the Rosebud. Figure II.D-6 compares two stages of in-stack collection for the Zap, and clearly shows the individual spheres. These photomicrographs also indicate the particle sizing ability of the cascade impactor.

To verify a difference in the ability of the starting material to "shed" ash, samples of Zap and Rosebud, pyrolysis chars were quantitatively combusted in the entrained flow reactor to various levels of burnoff. The partially combusted material was collected in a cyclone separator that would clean the char of the smaller released ash and any fragmented particles. TGA weight loss analysis was then performed on the combustion char to indicate the fraction of ash present in the particles, and from this, the percent ash retained from the starting material can be calculated by

$$\% \text{ ash retained} = \frac{\% \text{ combustion sample} \times \% \text{ ash in combustion sample}}{\% \text{ ash in starting material}}$$

Table II.D-2 presents the percent ash retained values for several levels of combustion. The data appears to indicate two points: 1) the samples shed to a relatively constant ash level early in the combustion process, and 2) the Zap initially sheds more of its ash than the Rosebud. Further tests will be done to see if a gradual release of ash occurs earlier in the combustion process; and to see if the extent of pre-charring effects this process.

To study the mineral matter to fly ash transformation, a comparison was made by SEM/dispersive x-ray analysis of the solidified ash spheres on the Zap char's surface with particles collected in the preseparator above the flame in the TWR. The ash spheres on the chars surface are rich in Ca, moderately rich in Al and Si and have varying amounts of Fe, K and Mg. Representative qualitative analyses for these particles are presented in Table II.D-3. It appears that the coal's organically bound calcium accumulates in the form of molten liquids, along with the fine clay and pyrite particles.

Figure II.d-7a shows a photomicrograph of particles collected above the flame. Some of these particles have melted to form spheres and some have not. Qualitative analyses of the numbered particles are presented in Table II.D-4. In the figure, samples 1 and 2, which appear to have melted and crystallized, are almost pure iron oxide. Figure II.d-7b shows a close-up of the highly

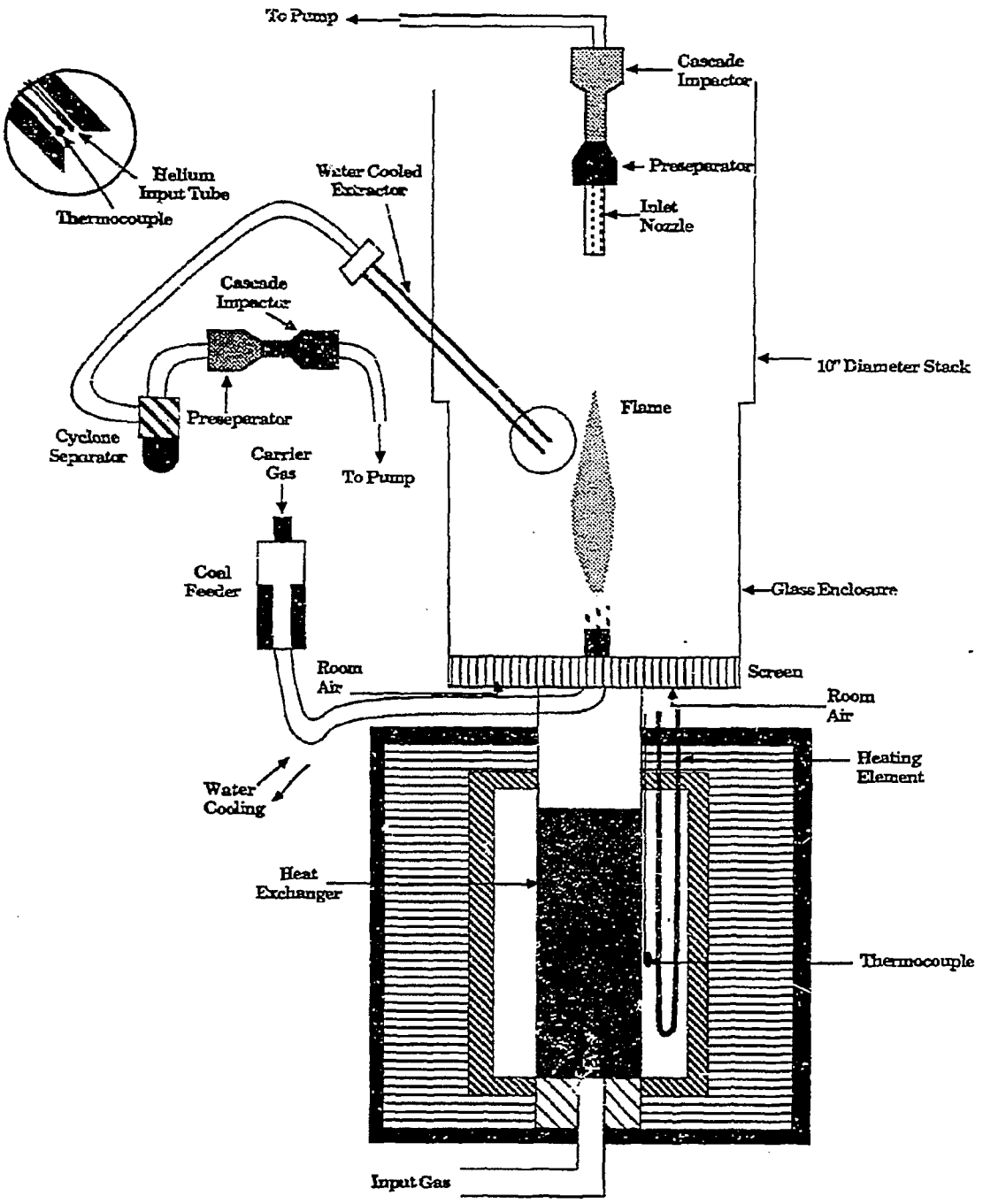

Figure II.D-1. Probes for Char and Ash Collection from the Transparent Wall Reactor.

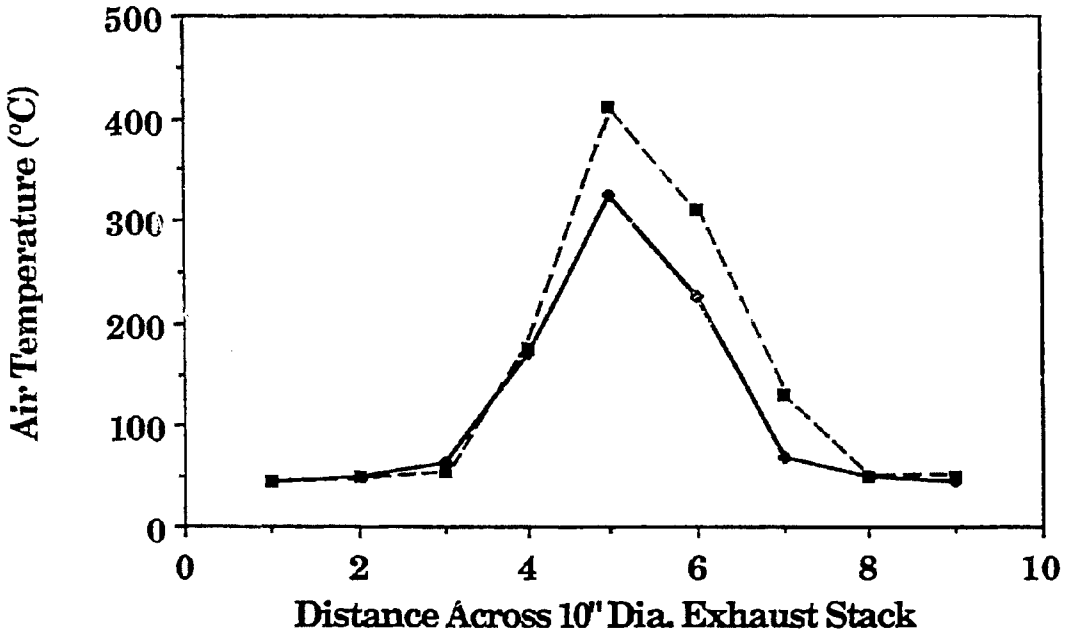

Figure II.D-2. Air Temperature Profile Across TWR Exhaust Stack with Rosebud (200x325) Flame On. Distance Above Injector: ■ , 70 cm; ◆ , 75 cm.

Table II.D-1. Sample Collection Data for Zap and Rosebud Flames.

						Percent Weight Loss in TGA*	
Run #	**Sample**	**% Ash**	**Collection Point**	**Collection Time Minutes**	**Wt. of Sample Collected (mg)**	**Cyclone Fraction**	**Preseparator Fraction**
1	200 x 325 Dry Rosebud	12.7	7 cm above Ignition Point (in flame)	2	356.0	62.24	---
4	200 x 325 Dry Zap	7.3	7 cm above Ignition Point (in flame)	3	158.8	59.42	---
2	200 x 325 Dry Rosebud	12.7	In Stack 75 cm above Injector	10	81.5	---	6.10
10	200 x 325 Dry Zap	7.3	In Stack 75 cm above Injector	20	22.1	---	3.43

* TGA analysis in air at 30K/min to 900°C

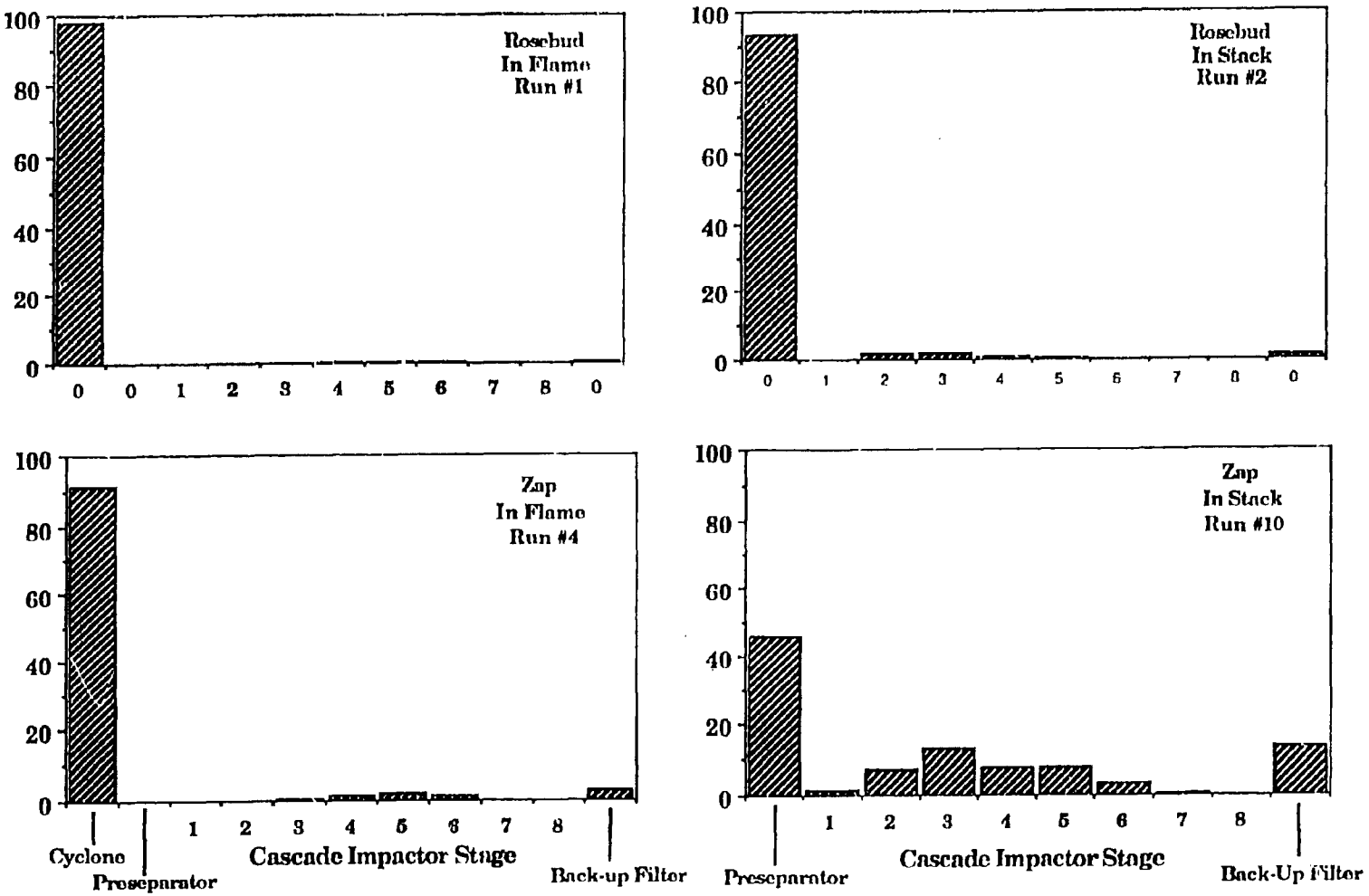

Figure II.D-3. Particle Separation Distributions for In Flame and In Stack Collections for Rosebud Subbituminous Coal and Zap Lignite.

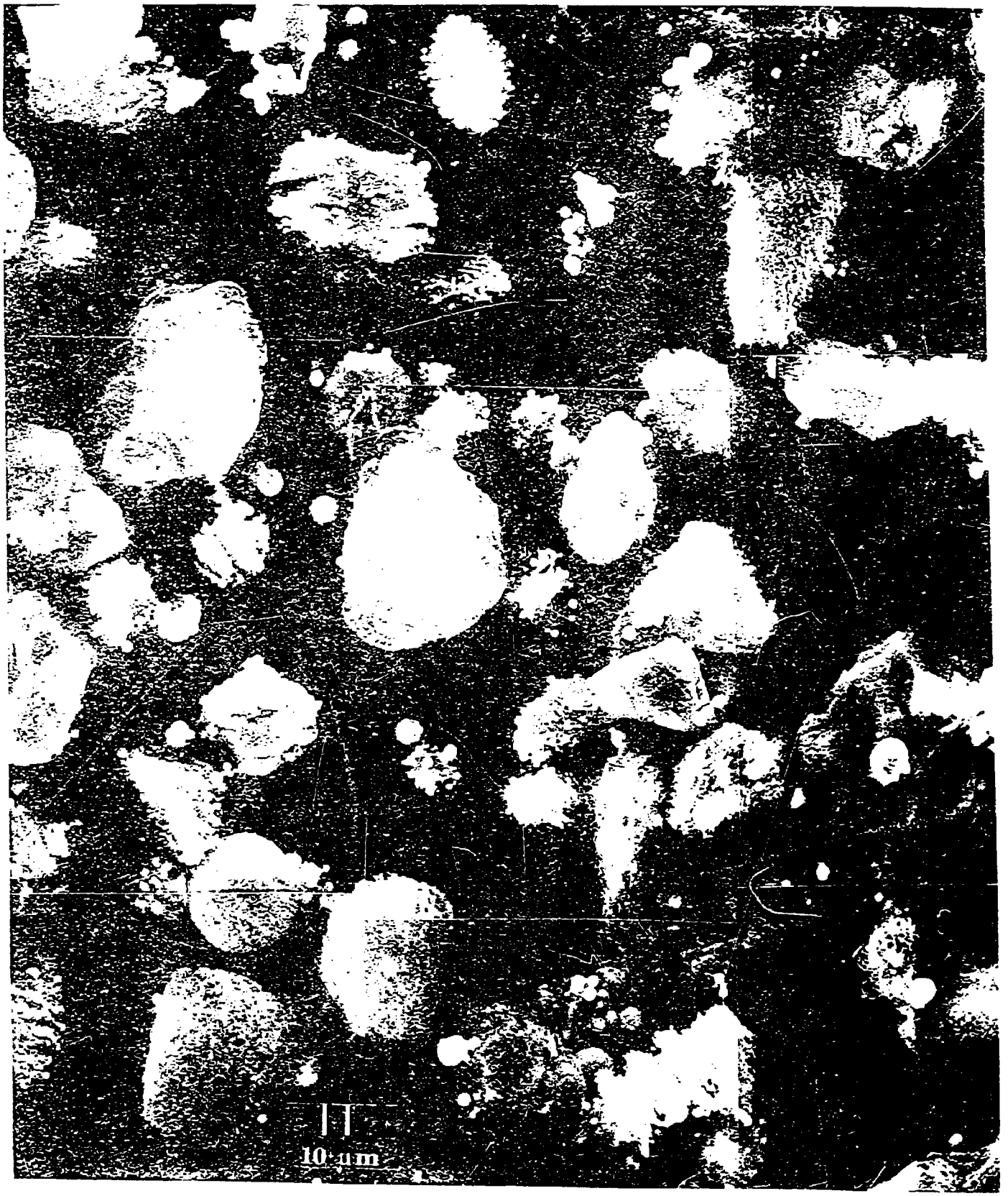
10 µm

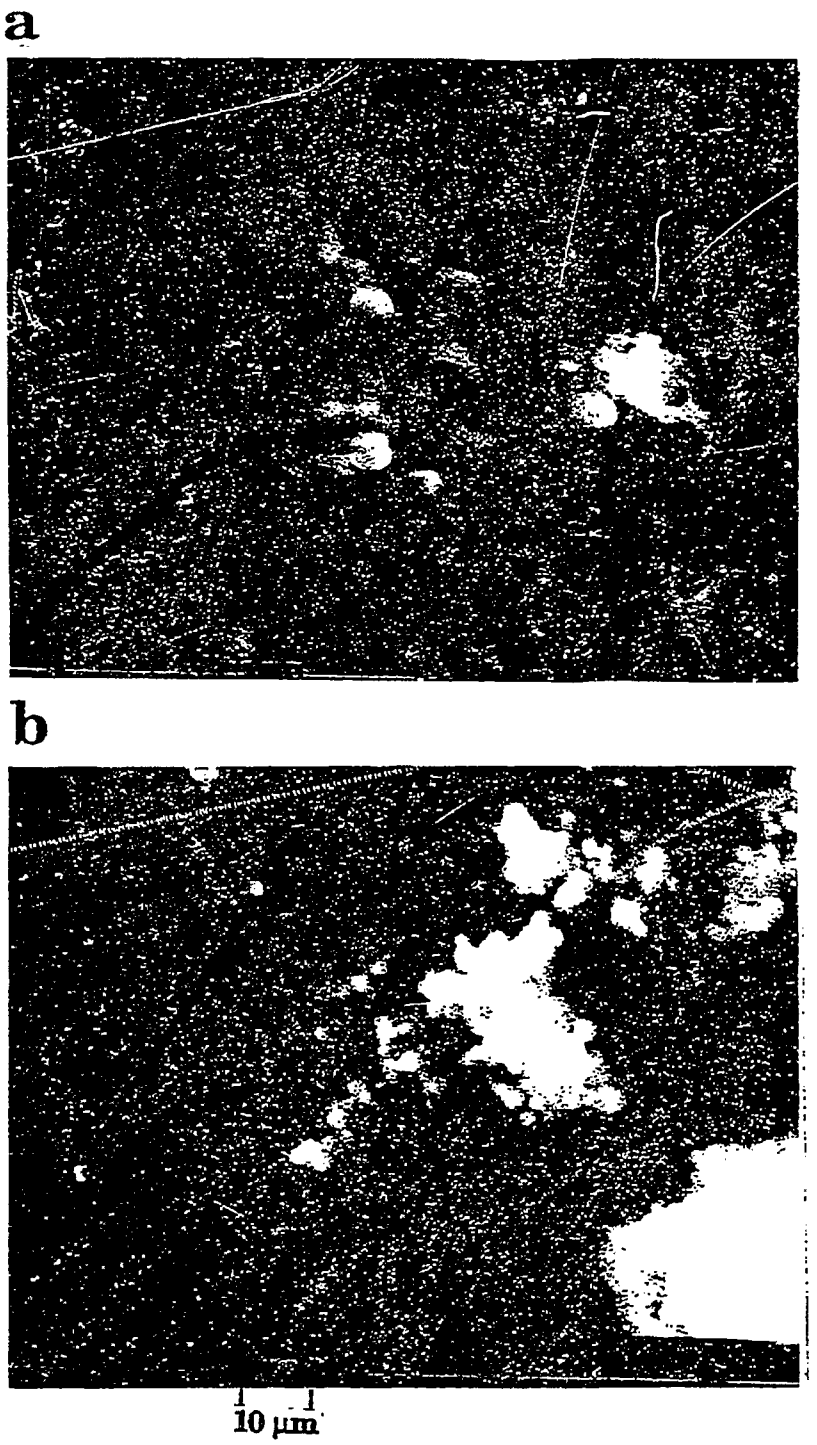

Figure II.D-6. SEM Photomicrographs of Fly Ash Collected Above a Zap Lignite Flame. a) Stage #2 and b) Stage #4 of Cascade Impactor. Magnification: X910.

Table II.D-2. Percent Ash Retained in Partially Combusted Samples.

Sample	% Sample Recovered after Partial Combustion	% Ash Retained
Zap*	39.0	44.7
	27.0	37.2
	16.5	40.0
	7.6	35.0
Rosebud**	66.7	66.1
	28.0	71.0
	22.3	75.4
	21.1	67.1

* 900°C Zap Char

** 1500°C Rosebud Char

TABLE II.D-3

REPRESENTATIVE QUALITATIVE* X-RAY ANALYSIS FOR ASH SPHERES ON CHAR PARTICLE SURFACES AS SHOWN IN FIG. II.D-5

Values are in weight percent

Mineral Component	A	B	C	D	E	F
Al	4.89	0.93	0.69	1.21	1.37	1.86
Si	6.10	0.85	5.05	0.56	1.78	1.49
Fe	0.65	3.47	0.73	0	0	1.21
Mg	2.70	1.45	1.21	1.53	1.53	3.31
Ca	5.86	11.71	3.31	2.22	2.66	6.62
Ti	0.52	0.08	0.04	0.04	0	0.20
Na	-	0	0	0	0.65	0
K	0	0	0.04	0.04	0.04	0
Sulfur (O)	0.16	0.12	1.05	0.08	0.56	0.48
Sulfur (M)	0	0	0	2.14	1.53	0
x in FeS_x	0	0	0	2	2	0
Total Ash	35.86	25.73	19.06	11.87	16.44	22.45

* Not matrix-corrected for coefficient of x-ray absorption for each component.

a

b

Figure II.D-7. SEM Micro Photograph of Fly Ash Collected Above a Zap Lignite Flame, Preseparator Fraction. a) X400 and b) Close-Up of Sample 1, X2,670.

TABLE II.D-4

QUALITATIVE* X-RAY ANALYSIS OF ASH PARTICLES PRESENTED IN FIG. II.D-7

Values are in weight percent

Mineral Component	1	2	3	4 (melted)	4 (not melted)	5	6	7	8	9
Al	0.23	0.19	0.36	12.18	2.52	2.20	9.78	0.84	9.13	9.55
Si	1.21	0.79	0.66	38.28	33.96	65.44	29.82	1.50	29.81	32.07
Fe	86.05	90.16	0.30	1.38	0.54	0.15	0.84	0.72	0.41	0.38
Mg	0.56	0.47	1.08	1.80	1.14	0.78	1.86	2.1	1.02	0.80
Ca	2.75	0.37	78.54	0.66	-	0.10	1.68	3.66	0.38	0.41
Ti	0	0	0.18	0.18	0.06	0	0.06	0.06	0.19	0.03
[illegible]	0	0	0	2.04	0	0	4.14	0	1.18	2.70
K	0	0.09	0	7.14	0.90	0	0.84	0	6.81	5.15
Sulfur (O)	0	0	0	0.06	0	0.05	0.06	0	0	0
Sulfur (M)	0	0	0.60	0	0	0	0	0	0	0
x in FeS_x	0	0	2	0	0	0	0	0	0	0
Total Ash	129.69	131.41	113.46	125.22	79.98	145.48	101.10	12.36	95.55	102.60

* Not matrix-corrected for coefficient of x-ray absorption for each component.

crystallized surface structure for these kinds of particles. Sample 3, which has not melted is almost pure calcite. Sample 4 shows a region which has not melted which is almost pure quartz, like sample 5, and a part which has melted which is a mixture of elements. Particles 1-5 appear to have been derived from individual extraneous mineral grains (pyrite, calcite, and quartz) without significant contamination by other mineral components. Small spheres (6 and 7, and those captured on the stages of the cascade impactor) as well as larger spheres (8 and 9) are mixtures of Si, Al, Ca, Fe, K and Mg, like the particles attached to the chars surface captured in the flame. Qualitative analysis of other particles similar in appearance to particles 1-9 are presented in the Fifth Quarterly Report (Table II.D-5).

Also of interest is that many of the pure mineral particles are of the same size (some larger) than the starting coal particles. Differences in color, magnetic attraction, and density (hollow vs. solid) have also been observed.

SEM/dispersive x-ray analysis was also performed on individual ash spheres that were recovered from the eight stages of the cascade impactor for an "in stack" ash collection from 200 x 325 mesh Zap lignite. As noted in the Fifth Quarterly Report for this program, the small spheres (< 10 μm in diameter) apparently are shed from the coal particles during the combustion process and contain inorganic components that are intrinsic to the coal. X-ray analysis was performed on the eight size fractionated samples to see if the inorganic species present were biased towards certain particle sizes.

For presumably pure mineral oxides, however, the x-ray data produced consisted of unusually low ash values: typically < 4% total ash. Investigation has led us to believe that due to the small particle sizes and the relatively high acceleration voltage (30 kv) used for the analysis, transmission and sidescatter of the penetrating electron beam through and out of the particles has become significant. This condition would result in x-rays being emitted by the substrate, a graphite layer, that has an atomic number too low for detection on our instrument and would result in the observed low material balance.

To correct for this condition, we will turn down the electron beam acceleration voltage, and also analyze some pure oxide standards in the same particle size range to better calibrate the instrument.

It was decided to move many of the ash collection experiments to the entrained flow reactor (EFR), a schematic of which is shown in Fig. II.D-8. This will allow the use of smaller quantities of coal and will provide for more complete collection of the ash.

Char Reactivity

The reactivity of chars prepared from both raw and demineralized coals was measured. The chars were prepared by heating in N_2 at 30°C/min until 900°C was achieved. The char reactivity measurements were made by employing a non-isothermal technique using a TGA. With an air flow of 40 cc/min and a N_2 purge flow of 40 cc/min, the samples were heated at a rate of 30°C/min until 900°C was reached. The resulting critical temperatures (defined as the temperature at which the derivative of the weight loss reaches 0.11 weight fraction/min) are plotted in Fig. II.D-9 as a function of oxygen in the parent coal.

The trend for the raw samples is an increase in reactivity (decreasing T_{cr}) with increasing coal oxygen content, while the slope for the demineralized samples seems to flatten out at approximately 520°C. Above 10% oxygen, the mineral content of the coal dominates the char reactivity, increasing the char's reactivity (lower

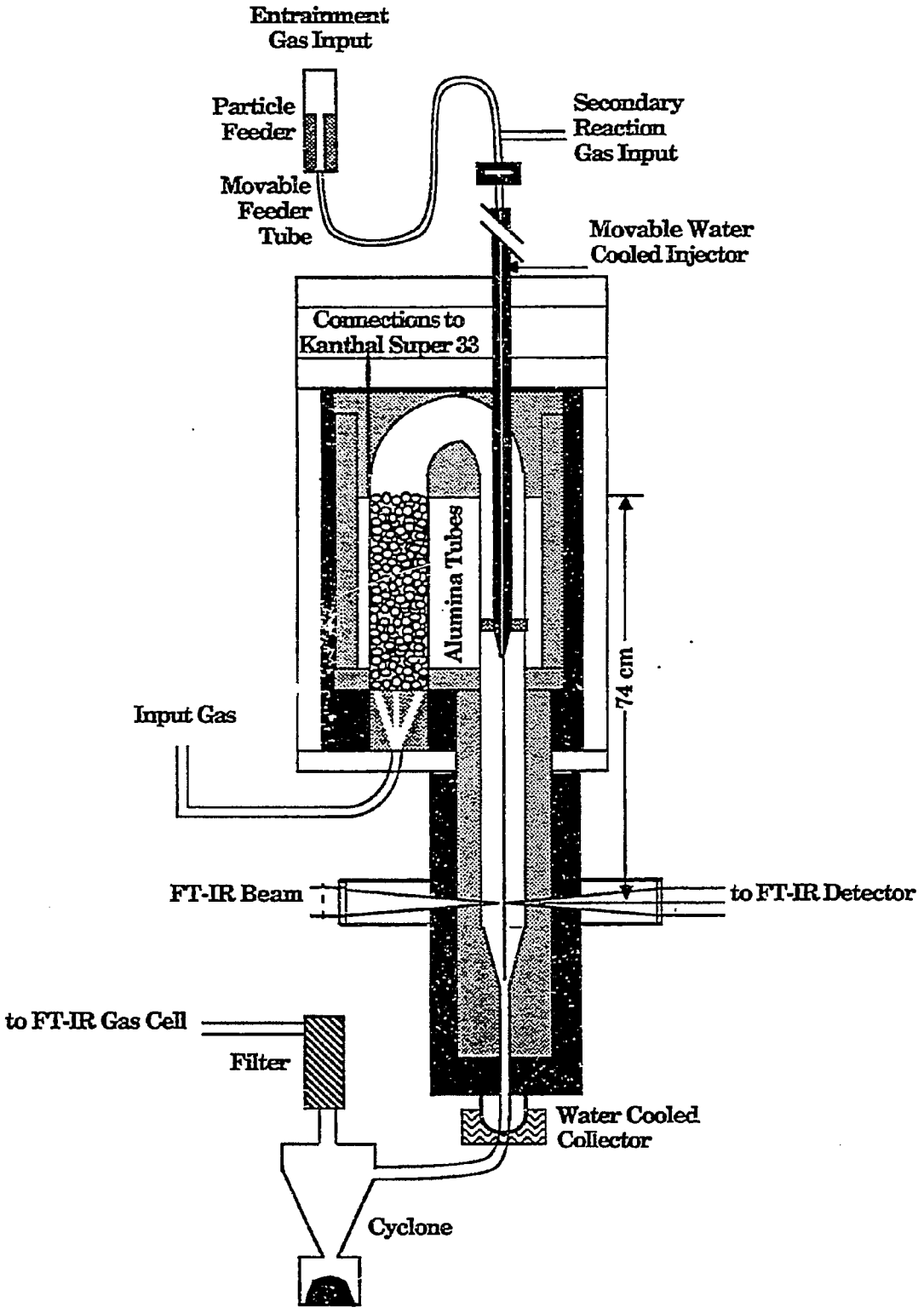

Figure II.D-8. Schematic of Ash Collection System Installed on the Entrained Flow Reactor.

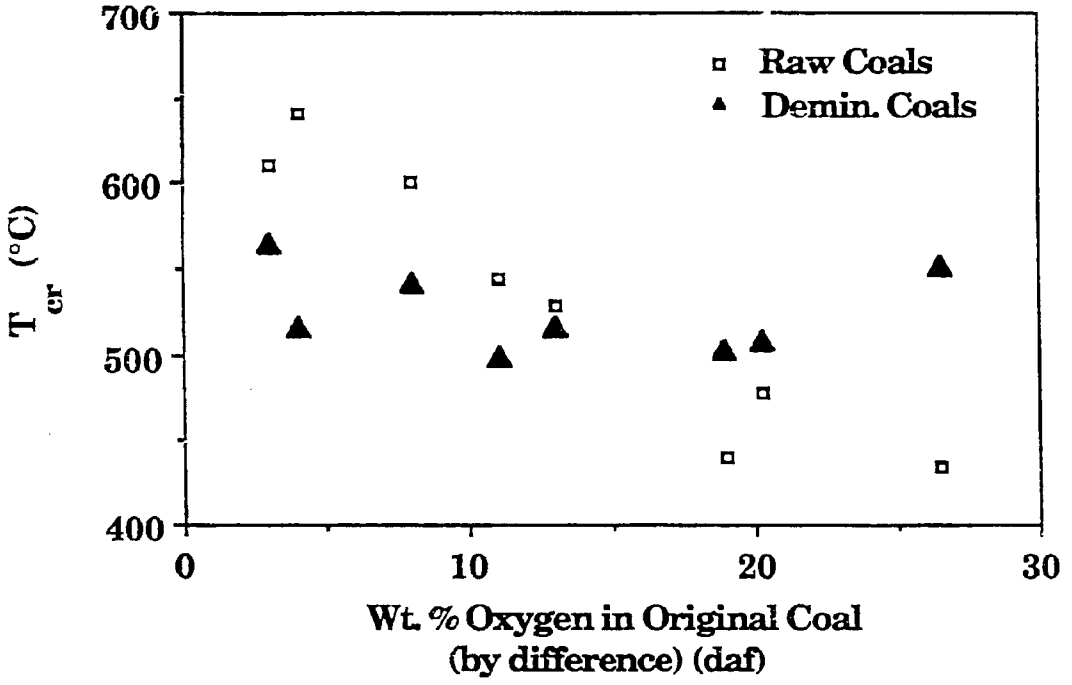

Figure II.D-9. Variation of Reactivity with Coal Oxygen Content for Raw and Demineralized Argonne Coals.

T_{cr}) compared to the demineralized samples. The reason for this increase appears to be the catalytic activity of the organically bound alkali metals, particularly the Ca since Ca is naturally abundant in coals. Below 10% oxygen content, the raw coals have a lower reactivity (higher T_{cr}) than the demineralized samples. The reason for this is not known and is being investigated.

In order to ascertain why there is a systematic increase in reactivity with coal oxygen content when reactivity is thought to depend on calcium content, the calcium concentration of coals from the Exxon sample bank were plotted as a function of oxygen concentrations in Fig. II.D-10. Above 8% oxygen, there is a systematic increase in Ca with increasing oxygen.

Eight percent is the level at which carboxyl groups appear in coal (Blom et al., 1957). This suggests that, above 8% oxygen content, there is a systematic increase in the amount of calcium ion-exchanged on the carboxyl groups and it is this calcium component which acts as a catalyst.

In order to further understand the roles played by the ion-exchangeable cations in char reactivity, a 200 x 325 mesh sieved fraction of Zap Indian Head, demineralized according to the standard Bishop and Ward (1958) technique, was subjected to ion-exchange with Ca, Mg, K, and Na using a modification of the procedure by Hengel and Walker (1984). The amount ion-exchanged onto the demineralized Zap lignite was controlled by using different molar solutions of the acetate salt. In the case of Ca, 1.5M, 1.0M, 0.5M, 0.3M, 0.1M, and 0.05M acetate salt solutions were employed. In the case of Mg, 1.5M and 0.05M acetate salt solutions were employed. In the case of K, 1.5M, 0.3M, 0.1M, and 0.04M acetate salt solutions were employed and in the case of Na, 1.5M, 0.3M, 0.1M and 0.05M acetate salt solutions were used. Slurries of 5 grams of demineralized Zap and 125 ml of the desired loading solution was stirred at 57°C for 5 1/2 hours. The solution was allowed to cool to room temperature and stirring was continued for an additional 22 1/2 hours. The slurry was filtered, washed with deionized water and dried at 105°C in a vacuum oven for approximately two hours. The amount of cation exchanged was determined by x-ray analysis.

Chars were prepared from the cation loaded coals by heating in N_2 at 30°C/min to 900°C and these were subjected to the non-isothermal reactivity test in air. The char from demineralized Zap coal is far less reactive (higher T_{cr}) than the raw Zap char. As previously discussed, this is probably due to the removal of the organically bound alkali metals which are thought to dominate char reactivity in coals possessing more than 10% oxygen. If this is true, then cation loading should result in the restoration of char reactivity.

Plotted in Fig. II.D-11 is the variation of reactivity with the cation loadings. The Ca and Mg loadings effectively restored the reactivity of the demineralized Zap. In the case of Ca, the only significant change in reactivity occurs when the Ca level increases from the 0.01 wt% in the raw demineralized Zap to 1.65 wt% in the 0.05M loading. Further increases in Ca do not cause any marked increases in reactivity. The low Na and K loadings were so effective in promoting the demineralized Zap char reactivity that the loaded samples yielded values of T_{cr} that were 45°C and 30°C respectively less than the T_{cr} of the raw Zap char itself. With higher loadings, however, both Na and K lost their ability to increase char reactivity (lower the T_{cr}) and actually demonstrated hindering effects. The 1.5 M Na and K loadings gave values of T_{cr} which were higher by 129°C and 85°C, respectively, than the demineralized Zap sample. Surface area measurements were done of the raw and cation-loaded samples in these cases. However, significant differences were not observed between the raw and cation-loaded coals in either case. Consequently, the hindering effect must manifest itself either during the

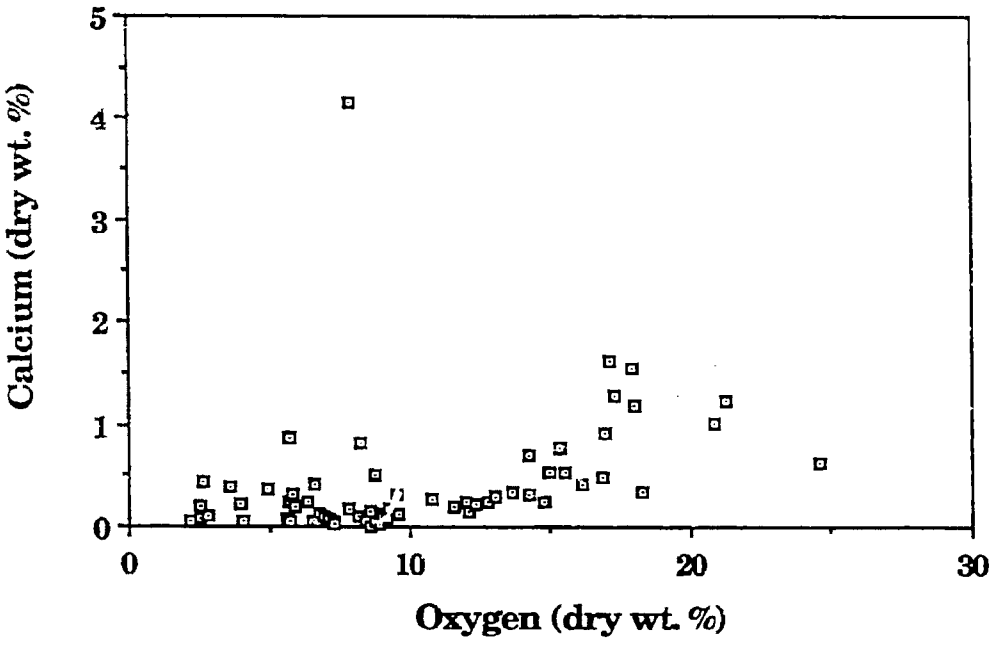

Figure II.D-10. Weight Percent Calcium as a Function of Oxygen in Coal.

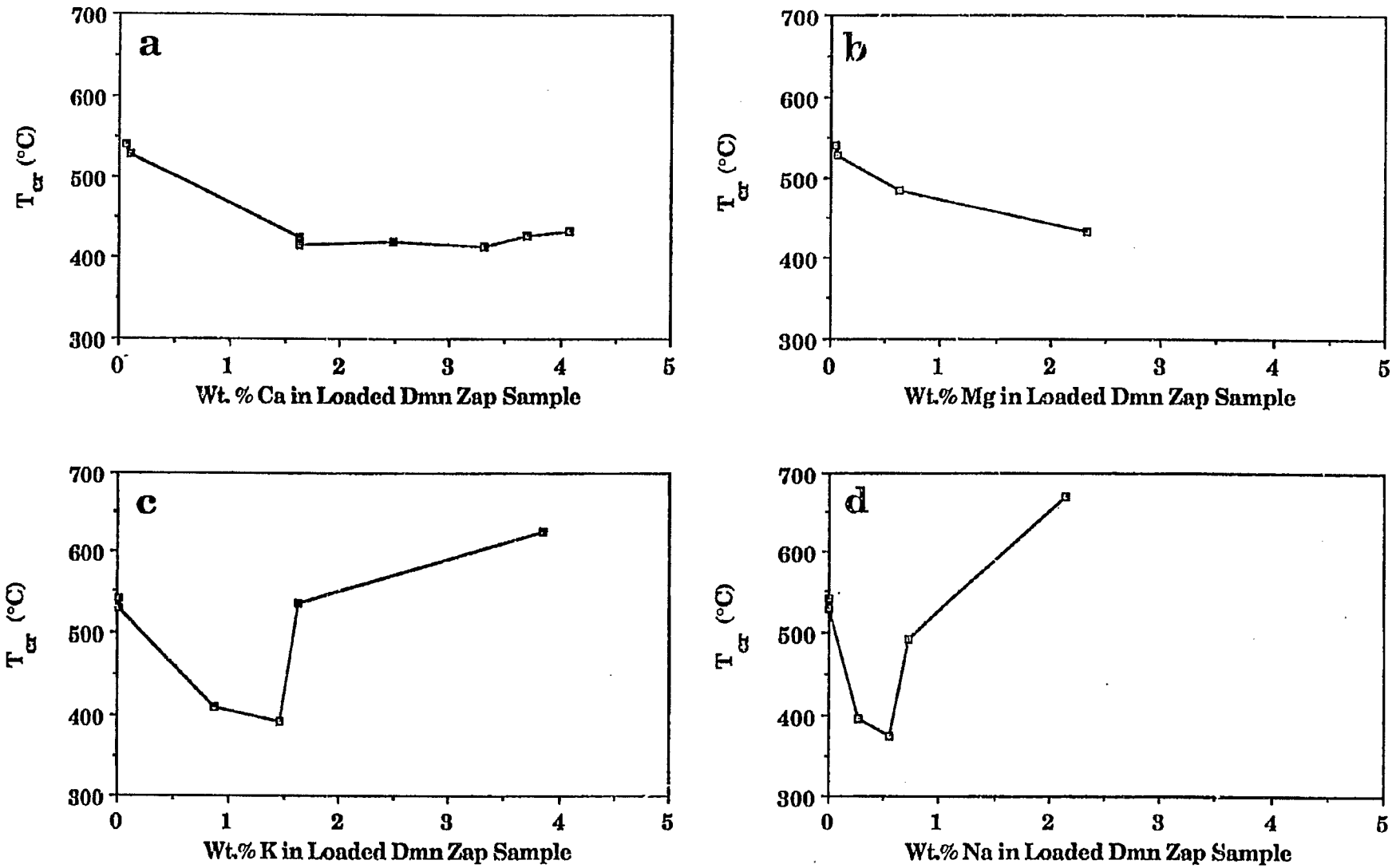

Figure II.D-11. Variation of Reactivity with Cation Loadings for Demineralized Zap Coal.
a) Calcium; b) Magnesium; c) Potassium; d) Sodium.

char formation process or the gasification process. It is planned to check the first possibility by doing pyrolysis experiments with cation-loaded samples in a reactor which can handle samples which are large enough to allow surface area measurements on the resultant char. The second possibility will be investigated by doing temperature programmed desorption (TPD) experiments on chars produced from raw, cation-loaded and demineralized coals.

Although most of the work in the past year dealt with char reactivity in air, CO_2 char reactivity measurements were done on chars produced from raw, demineralized and loaded demineralized Zap samples by heating in N_2 at 30°C/min until 1000°C was achieved. The CO_2 reactivities followed similar trends as the air reactivities as shown in Fig. II.D-12.

A model was developed to predict the intrinsic reactivity (T_{cr}) of char based on calcium content for coals greater than 10% oxygen, while holding the extent of pyrolysis and heating rate constant. For a standard test:

$$T_{cr} = 520 + \alpha\,(\text{Ca wt\%} - (\beta * \text{carbonate})) \qquad \text{(II.D-1)}$$

where, 520 represents the approximate T_{cr} for demineralized coals, α is the slope from the plot of T_{cr} vs Ca wt% in Fig. II.D-11a, β is a constant and the carbonate value is that obtained from quantitative FT-IR analysis.

Figure II.D-13a displays the correlation between actual T_{cr} and predicted T_{cr} with $\beta = 0$. Since it is the organically bound Ca which is thought to be catalytically active, a much better correlation is obtained when calcite corrections are included in the model (Fig. II.D-13b).

In order to better understand why the organically bound Ca offers catalytic activity and calcite does not, SEM Ca dot maps were done for a calcium loaded demineralized. Zap coal and an Exxon sample which, from FT-IR analysis, was known to be abundant in calcite. The maps in Fig. II.D-14 indicate that the organically bound Ca is very well distributed throughout the Zap coal while the calcite in the Exxon coal exists in large clusters. This is consistent with the fact that the Ca in the calcite form is not nearly as effective as a catalyst when compared to the ion-exchanged Ca. However, it is also true that even if the calcite were well-distributed, it may not promote gasification reactions.

Plans

Continue collection and characterization of ash particles produced in the TWR. Modify a new version of the EFR to study ash transformations for a wide range of coals at different levels of burnoff.

Continue study of mineral effects on the reactivity of coals and chars toward air or CO_2, particularly with regard to how minerals effect reactivity and char formation processes for medium and high rank coals.

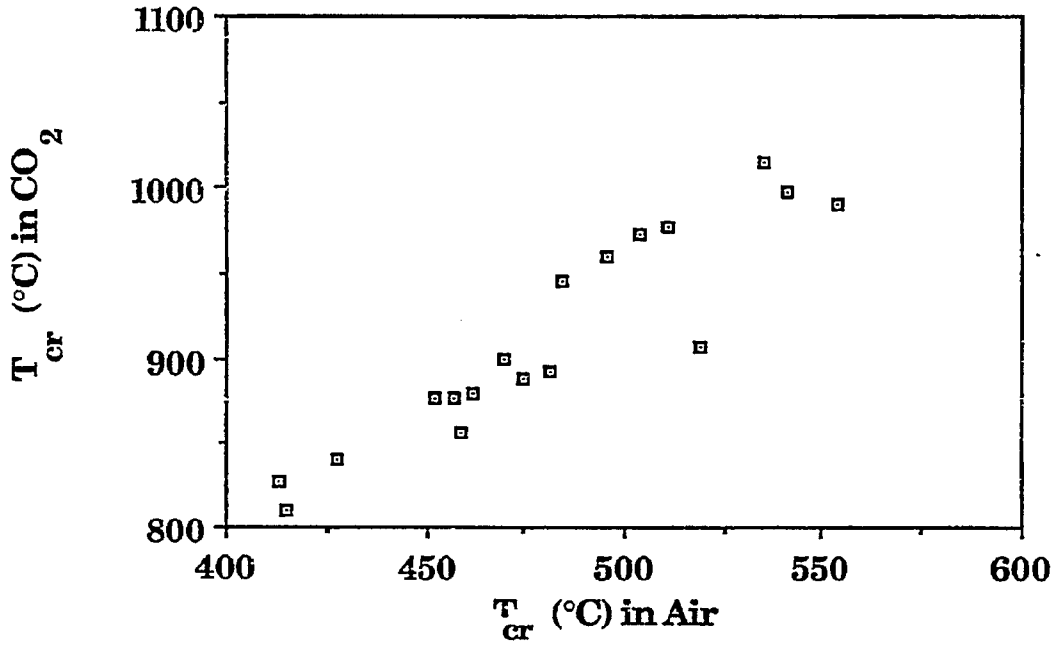

Figure II.D-12. Correlation Between CO_2 and Air Reactivity Parameters

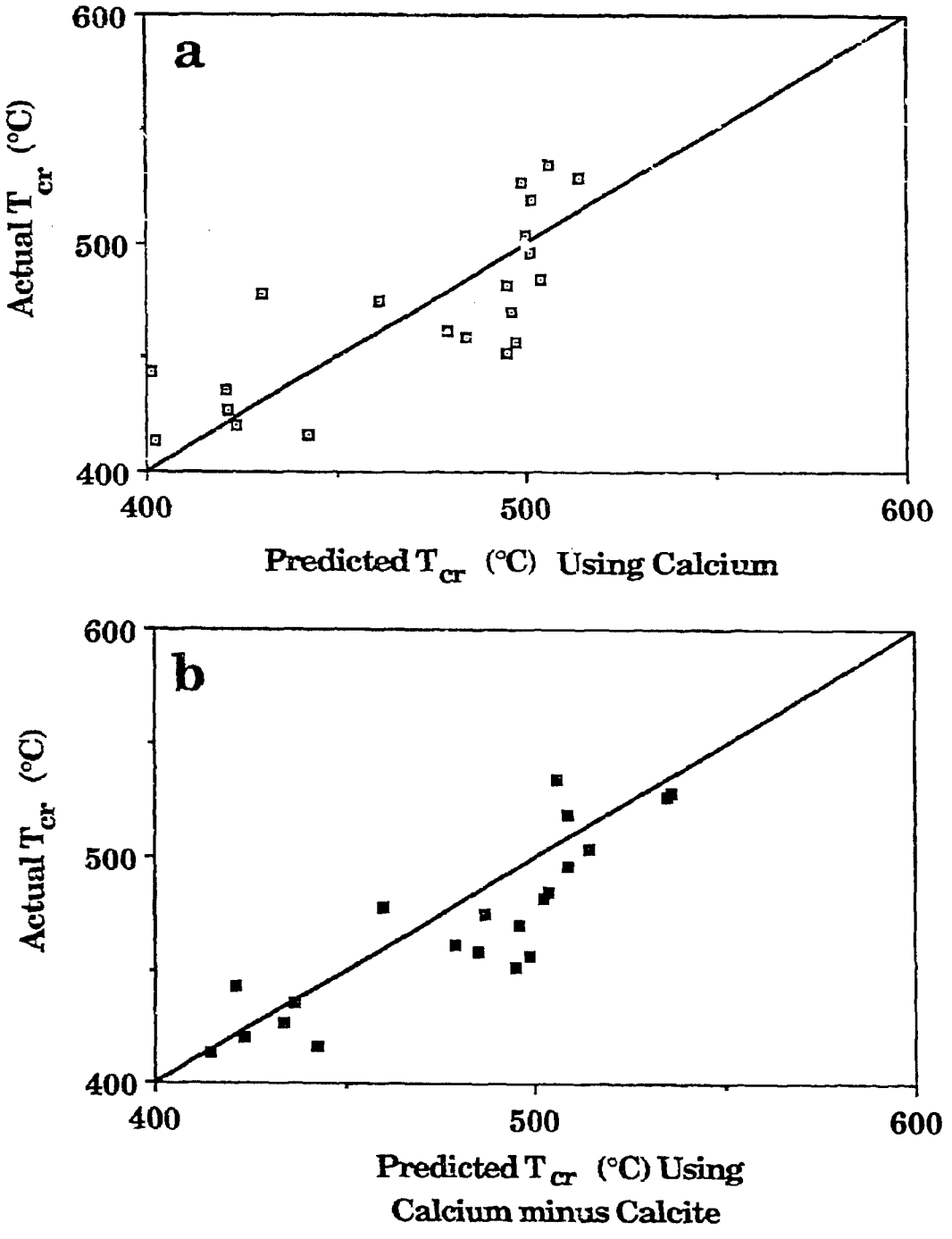

Figure II.D-13. Correlation Between Actual Reactivity and Predicted Reactivity Based on Ca Content. a) with Calcite; b) Without Calcite.

a

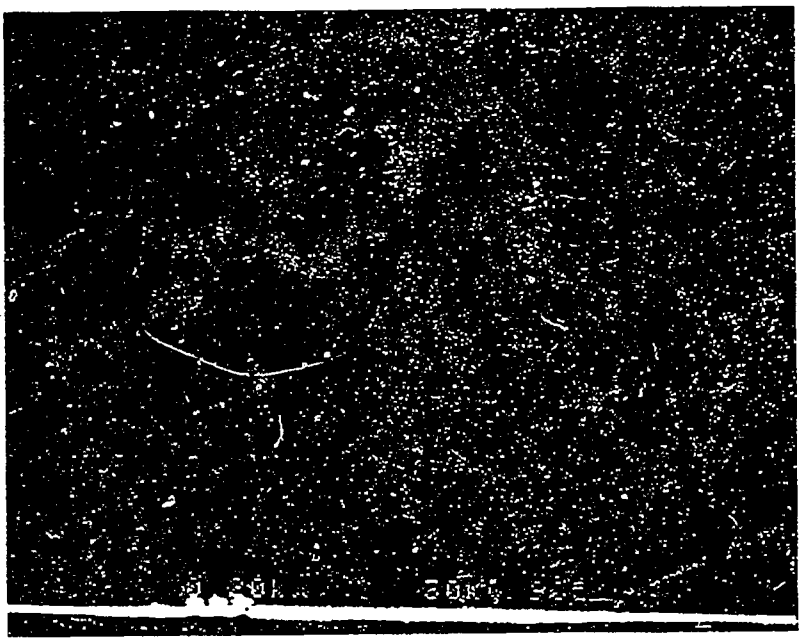

b

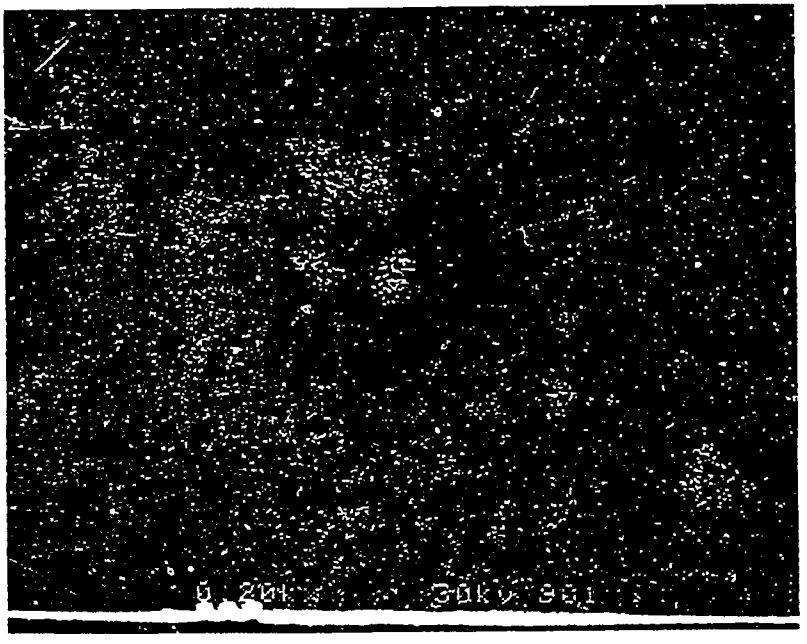

Figure II.D-14. SEM Calcium Dot Maps. a) Ca Loaded Demineralized Zap Coal, No Calcite; b) Exxon #6 Coal, High Calcite.

II.E. SUBTASK 2.e. - LARGE PARTICLE SUBMODELS

Senior Investigator - Michael A. Serio
Advanced Fuel Research, Inc.
87 Church Street
East Hartford, CT 06108
(203) 528-9806

Objective

The objectives of this task are to develop or adapt advanced physics and chemistry submodels for the reactions of "large" coal particles (i.e., particles with significant heat and/or mass transport limitations) and to validate the submodels by comparison with laboratory scale experiments. The result will be coal chemistry and physics submodels which can be integrated into the fixed-bed (or moving-bed) gasifier code to be developed by BYU in Subtask 3.b. Consequently, this task will be closely coordinated with Subtask 3.b.

Accomplishments

A literature review of heat and mass transport effects in coal pyrolysis was completed. A critical evaluation was made of two models from the literature that have been used to describe coupled reaction and transport in large particles. The formulation of our own single particle model was begun. Discussions were also held with BYU on the interface between the single particle model and the advanced fixed bed reactor model.

The design and construction of a small scale fixed-bed reactor was completed. This reactor will have on-line analysis of evolved volatile products and on-line measurement of char functional group composition and particle temperature.

Evaluation of Pyrolysis Heat/Mass Transport Models

During the past quarter, a more detailed examination was made of the models of Devanathan and Saxena (1985,1987) and Bliek et al. (1985) in order to choose a starting point for a model of large particle pyrolysis.

The original model of Devanathan and Saxena (1985) was developed for the devolatilization of large non-plastic coal particles. Their objective was to develop a comprehensive pyrolysis model considering heat and mass transport resistances. Since the primary focus of their work was the effects of the transport parameters, the initial (Devanathan and Saxena, 1985) paper used a simple single-reaction model with a global activation energy for primary pyrolysis. They also ignored the temperature variation of the physical properties (heat capacity, thermal conductivity). The latter simplification is a major weakness of their approach, but can be easily remedied. In addition, they assumed pyrolysis is thermally neutral, which is probably not a bad assumption, as discussed in the Second Quarterly Report.

This model was developed to describe non-plastic coals which largely retain their pore structure during pyrolysis. The volatile species were lumped into a single component. An effective diffusion coefficient was assumed to account for volatile transport by diffusion and convective flow under small pressure gradients.

The pyrolysis reaction in this model is represented by:

$$C\ (Coal) \xrightarrow{\quad} A(Volatiles) + S(Char)$$

The nonlinear partial differential equations obtained for the material and energy balances were solved using the DPDES routine of IMSL. This routine uses the method of lines which reduces the system of partial differential equations into a system of ordinary differential equations, which are subsequently solved with a Gear Integration method. The equations were solved for various values of the Thiele modulus, corresponding to high, medium and low reaction rates.

Using an assumed set of kinetics, thermal properties and diffusion coefficients, they identified regimes of chemical reaction control (at low reaction rates), and heat and mass transfer control (at high reaction rates). By doing parametric studies they identified the Thiele modulus (chemical reaction rate/diffusion rate), the Lewis number (thermal diffusivity/mass diffusivity) and the heat transfer Biot number (ratio of external to internal heat transfer rate) as important dimensionless groups. The analogous mass transfer Biot number was found to be unimportant since the external film resistance was assumed to be negligible.

A second paper (Devanathan and Saxena, 1987) extended the model to include secondary reactions. The description of the volatiles was also extended to three components (tar, gas, hydrogen). The global primary and secondary pyrolysis reactions were:

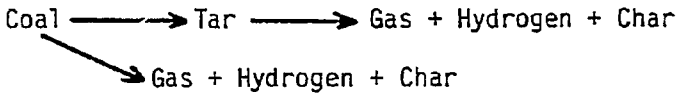

In this paper, Devanathan and Saxena used the primary pyrolysis kinetic parameters of Suuberg et al. (1978) instead of the parameters of Kobayashi et al. (1977) used in the previous paper. This change was presumably to accommodate a multi-component pyrolysis model. However, it is surprising that the authors do not comment on the significantly higher kinetic rates implied by the former set of parameters. Again, the physical properties were assumed to be constant, the heat of reaction assumed to be zero, and the mass transfer model utilized an effective diffusion coefficient to account for volatile transport both by molecular diffusion and convective flow under a small pressure gradient. It was also assumed that tar was only present in the vapor phase. The kinetics for the tar decomposition reaction were based on the values assumed by Suuberg et al. (1979). The numerical scheme used to solve the set of 7 partial differential equations for a 3-component system was a similar technique as discussed above.

The authors used the expanded model to examine the effects of bulk temperature, pressure, and particle size on the extent of secondary reactions and volatile yields. Qualitative comparisons were made to the data of Suuberg et al. (1978) for Montana Lignite for the effect of pressure, temperature and particle size. Comparisons were made to the data of Stubington and Sumaryono (1984) for product evolution profiles from large particles. The simulations indicated two peaks in the H_2 evolution curve in agreement with Stubington and Sumaryono (1984). The first peak in the model was due to primary pyrolysis reactions while the second was due to tar decomposition.

One weakness of their approach is that the secondary reactions of tar outside the particle are ignored so that the predictions which show tar yield leveling off at relatively high temperatures do not make sense. They also predict a temperature of 750°C for the maximum tar yield, which is 150-200°C higher than most experimental observations. By assuming an inverse relation of the diffusion coefficient with pressure, they can predict the type of pressure dependence indicated by the data of Suuberg et al. (1978). One interesting prediction of their model is the fact that the pressure dependence is more prominent in the later stages of devolatilization since the volatiles have to travel a further

distance to get to the surface.

The total volatile yield was found to depend weakly on particle size while the total devolatilization time was found to depend strongly on particle size. These particle size trends, as well as the trends with pressure and temperature discussed above are in qualitative agreement with literature results. However, when quantitative comparisons are made, such as the temperature for maximum tar yield, the predictions are often far off, as noted above. This is a result of the fact that the physical and chemical parameters which go into the model were selected somewhat arbitrarily. The authors did note that some of these parameters could not be estimated accurately and did a sensitivity analysis on the external heat transfer coefficient, thermal diffusivity, external mass-transfer coefficient, effective diffusion coefficient and porosity. Of this set, the choice of the effective internal diffusion coefficient was found to be crucial. This parameter is also one the most difficult to specify. Unfortunately, the authors did not examine the sensitivity to the kinetic parameters.

A comprehensive model for large particle pyrolysis was also developed by Bliek et al. (1985). They used essentially the same global pyrolysis scheme (including tar secondary reactions) as Devanathan and Saxena (1987). One difference in the kinetic models was to assume that each of the three volatile components evolves by a reaction which is second-order in the amount of volatiles yet to be released. This is a simpler alternative to the distributed activation energies model to describe the "tailing" of volatile evolution curves at higher temperatures. This model also treats coals which essentially retain their pore structure.

One of the major differences of this model when compared to that of Devanathan and Saxena (1987) is in the treatment of internal mass transfer. Bliek et al. chose to use the continuum limit of the Dusty Gas model (Mason et al., 1967; Mason and Malinauskas, 1983). This model can account for the combined transport of volatiles by viscous flow and diffusion. Viscous flow becomes more important as the particle size increases, so this approach should be applicable over a wider range of particle sizes. The model requires an estimate of the viscous permeability, the effective Knudsen diffusivity, and the effect binary diffusivity. The latter quantity also appeared in the diffusive mass transport model of Devanathan and Saxena (1987). Bliek et al. (1985) used literature values of permeability parameters obtained from stationary mass flux experiments.

The transport of volatiles from the particle outer boundary to the ambient gas was assumed to be infinitely fast. This assumption is probably alright for light gases but not for heavy tars. The heat of devolatilization was assumed to be zero as did the Devanathan and Saxena (D-S) model. Unlike the D-S model, Bliek et al. did not concern themselves with the details of external heat transfer and specified the particle surface temperature. However, they did account for the temperature variation of the particle thermal conductivity and heat capacity, which the D-S model does not include. Bliek et al. also did pyrolysis experiments in a TGA with particles 50-1000 microns in size in order to extract primary pyrolysis kinetic information and generate data for model validation. The equations were solved numerically using an implicit backward descretization scheme. This transformed the partial differential equations to non-linear algebraic equations, which were subsequently linearized. A combination of iteration and the algebra of diagonal matrices was used to produce the numerical results.

The qualitative results of the simulations largely agree with those of the D-S model since both were developed to agree with the experimental observations of Suuberg et al. (1978), among others. The more detailed description of mass transfer allowed Bliek et al. to establish regimes of particle size and heating rate where mass transfer was controlled by either diffusion or viscous flow. The

most interesting prediction was that the tar yield went through a maximum with heating rate. This was explained by the fact that at high heating rates, the volatiles would have to diffuse through a hot outer layer of char. However, this trend has not been observed experimentally. The model also did not agree well with the effects of ambient pressure observed for bituminous coal by Anthony and Howard (1976). However, this could be due to the fact that it was developed for a non-plastic coal.

While both the Bliek model and the D-S model are important contributions to understanding large particle pyrolysis, the published versions are lacking in several respects. The major problem is the relative lack of care which has gone into the choice of the physical and kinetic parameters. A corresponding defect is the lack of a complete sensitivity analysis. If we compare the choices of physical and chemical parameters made for the two models, which are shown in Tables II.E-1 and II.E-2, respectively, the magnitude of the problem is apparent. For example, there are several orders of magnitude variation in the species diffusivities. As discussed above, this was identified as a crucial parameter in the partial sensitivity analysis done by Devanathan and Saxena (1987).

Additional problems with these two models include an oversimplified description of tar secondary reactions, and the inability to describe plastic coals. We plan to address these and other deficiencies in our large particle model development.

Design of Fixed-Bed Reactor

Several different design configurations were considered for the fixed-bed reactor (FBR). These were narrowed down until a single design approach was agreed upon and then a more detailed design was developed. A schematic of the FBR is shown in Fig. II.E-1.

In this system, 0.5 - 3g of coal (0.5 - 3mm particle size) will be placed on the sample holder (5). The sample holder can be accessed by removing the window (7) and taking out the upper part of the joint (5). The sample holder is a 31 mm I.D., 25 mm long quartz tube. It is heated by a hot stream of gas produced in an electric preheater (1) which can also produce steam by the introduction of water. The preheated gas is forced to pass through the sample by making the path through the sample the only way for gas to exit the reactor.

The composition of the product gases and tar are measured in the cell (4) using FT-IR transmission. The temperature of the coal surface is measured by an emission FT-IR method through a window (7) using either a separate FT-IR spectrometer or the same one used for the transmission measurements. To be able to measure the surface composition and temperature of the coal particles, an additional IR source (D) is required. By switching on the IR source (D) (opening a shutter), the emission spectrum will contain the diffuse reflectance spectrum together with the emissivity spectrum of the same particle or particles. By closing the shutter, we measure emissivity only. The diffuse reflectance spectrum will be the difference of the two spectra.

Initially, the plan is to use two separate spectrometers. An IBM IR/32 with an IBM PC/AT will be used for the evolved gas analysis (EGA). The PC/AT will also provide the temperature programming and data handling capability developed at AFR for the TG-FTIR instrument. A second spectrometer, either on IBM IR/32 or a Nicolet 20SX, will be used for the emission/diffuse reflectance measurements.

Table II.E-1. Comparison of Physical Parameters for Two Pyrolysis Reaction / Transport Models.

Property	Units	Devanathan and Saxena (1987) 25°C	500°C	Blick et al. (1985) 25°C	500°C
Thermal Conductivity	cal/(cm s K)	5.497×10^{-4}		4.45×10^{-4}	
Heat Capacity	cal/(g K)	0.916		0.27	0.51
Density	g/cm^3	1.5		0.9	
Thermal Diffusivity	cm^2/s	4×10^{-4}		1.8×10^{-3}	9.7×10^{-3}
Gas Molecular Weight	g/g-mol	30		20	
Tar Molecular Weight	g/g-mol	216		325	
H_2 Diffusivity	cm^2/s	4×10^{-3}		---	
Gas Diffusivity	cm^2/s	4×10^{-4}		4.2×10^{-1}	3.2×10^{-1}
Tar Diffusivity	cm^2/s	4×10^{-5}		4.2×10^{-1}	3.2×10^{-1}
Coal Porosity	---	0.4		0.10	
Char Porosity	---			0.25	

Table II.E-2. Comparison of Kinetic Parameters for Two Pyrolysis Reaction / Transport Models.

			Devanathan and Saxena (1987)	Bliek et al. (1985)
V_1	(ultimate yield of H_2)	g/g	0.005	0.000
V_2	(ultimate yield of gas)	g/g	0.381	0.358
V_3	(ultimate yield of tar)	g/g	0.054	0.160
f_4	fraction of tar which can react		1.0	1.0
k_{01}	preexponential	s^{-1}	10^{18}	---
k_{02}	preexponential	s^{-1}	10^{12}	8.0×10^{4}
k_{03}	preexponential	s^{-1}	10^{17}	7.6×10^{11}
k_{04}	preexponential	s^{-1}	10^{13}	2.7×10^{4}
E_1		kcal/mole	80	---
E_2		kcal/mole	50	22
E_3		kcal/mole	75	37
E_4		kcal/mole	65	14

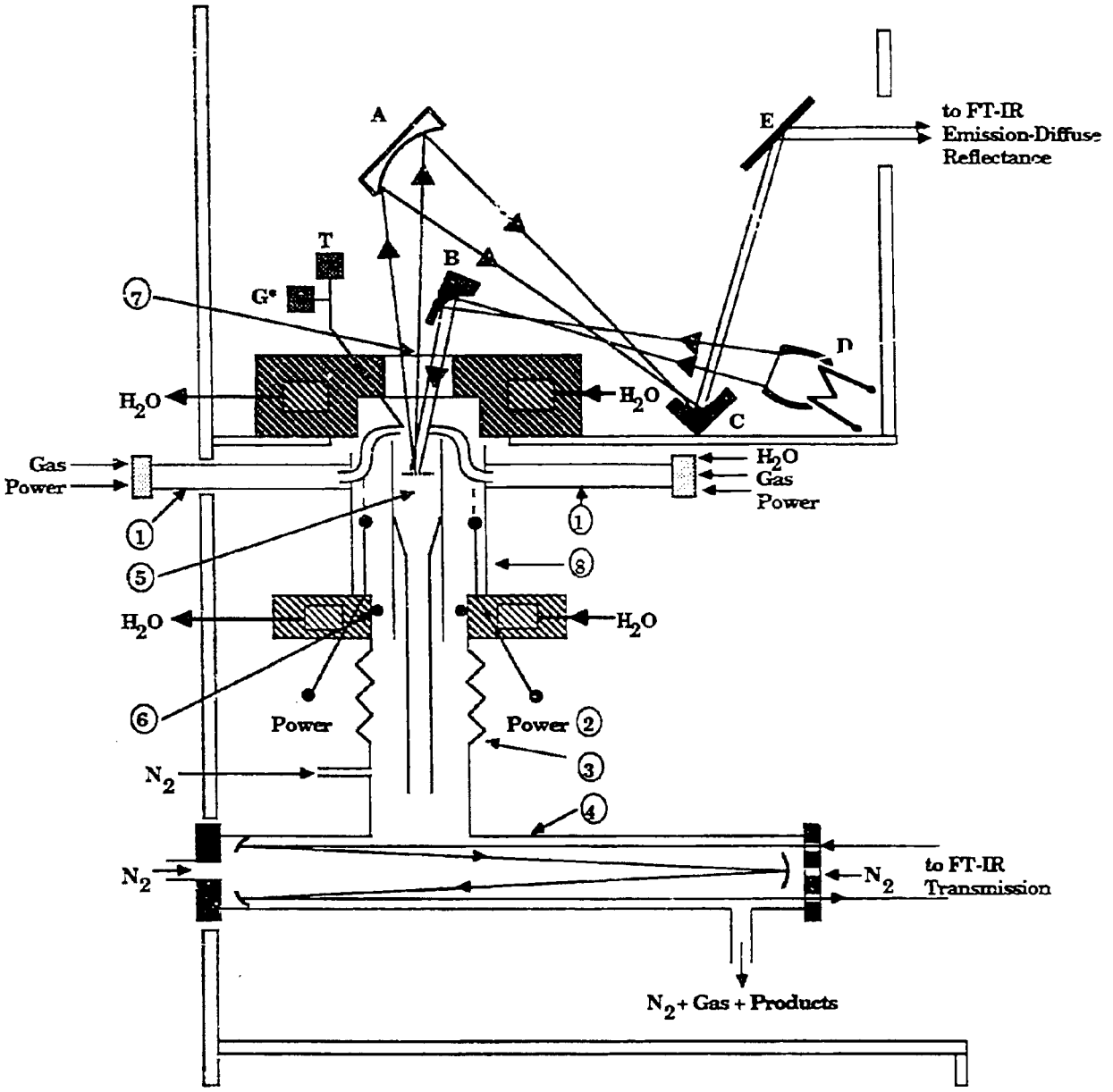

Mirrors

A: 4" Concave Mirror
B, C: Off-axis Parabola Mirrors
D: Ellipsoid Reflector with the IR Source
E: Flat Mirror

T: Thermocouple
G*: Port for Injecting Small Amounts of Reactives (O_2, CO_2)

1. Gas Preheater, H_2O Evaporator
2. Power to Additional Heater
3. Metal Bellows-Glass Connector
4. Dual Pass Cell
5. Quartz Reactor Tube (I.D. 1.18") with Grid to Hold Coal Sample
6. Vyton O-ring Seal
7. KBr Window
8. Outer Reactor Tube

Figure II.E-1. Schematic Diagram of the Fixed-Bed Reactor System.

Interface of Single Particle and Reactor Models

Historically, some fixed-bed gasifier models have assumed the devolatilization process to be instantaneous. Others have included finite rates for devolatilization and secondary reactions. The literature review by BYU identified three properties the devolatilization model should be able to predict: 1) the individual chemical species that will be evolved; 2) the amount of each that will be evolved; 3) the rate at which each will be evolved as a function of the pertinent variables (particle size, temperature, heating rate, pressure, gas velocity).

Currently, the FG-DVC model does a good job of predicting the kinetics and yields for the major products for a specified time-temperature history and pressure. What will be required for the fixed-bed model is to describe the devolatilization of large particles which may have significant internal gradients because of their large size and/or may react at significantly different times because of the broad size distribution of particles. These two effects could be accounted for by using a set of representative particles of different sizes as is done in PCGC-2. Instead of different trajectories the model would need to account for particles at different radial positions. This concept is shown schematically in Fig. II.E-2. One could also use continuous distribution functions instead of discrete distributions for particle size and location.

Other areas to be addressed include multiple particle effects, such as agglomeration, the secondary reactions of tar in the vapor space and on external surfaces, and the char reactivity. It may be possible to ignore agglomeration since most fixed-bed reactors have mechanical devices to prevent this. However, agglomeration may be important in mild gasification processes. Because of the lack of appropriate data, it is difficult to say how the secondary cracking of tar on surfaces should be treated. it is hoped that sufficient data to describe this phenomena will be generated under this subtask (2.e). The description of char reactivity will be an extension of the work done on smaller particles under subtask 2.a.

Discussions were held at AFR during the year quarter between Predrag Radulovic of BYU and Michael Serio, Peter Solomon, and Zhen-Zhong Yu of AFR regarding the interface between the Single Particle Devolatilization Model and the Fixed-Bed Reactor model. The consensus was that the interface would be very similar to that between the FG-DVC model and the 87 version of the PCGC-2. The major differences would be the requirement for a non-isothermal particle temperature model. The major area of uncertainty is how to efficiently integrate the non-isothermal particle model with the FG-DVC model to provide an "averaged" pyrolysis product distribution and char reactivity for large particles. As the two models are developed in parallel, a sensitivity analysis will help define what information should be exchanged and the degree of sophistication required. It was generally agreed that the amount of calculation time for the pyrolysis model should be less than 25% of the total.

This meeting also addressed the differences which may be required in the case of modeling a fixed-bed mild gasification unit, which are likely to be transient, batch systems with stronger particle interactions. The model will need to be flexible enough to cover these situations.

The exchange of information between the two models is summarized in Fig. II.E-3. The single particle model is AFR's responsibility. All of the "satellite" submodels in Fig. II.E-3 are BYU's responsibility except for those

Top View of Fixed-Bed Reactor

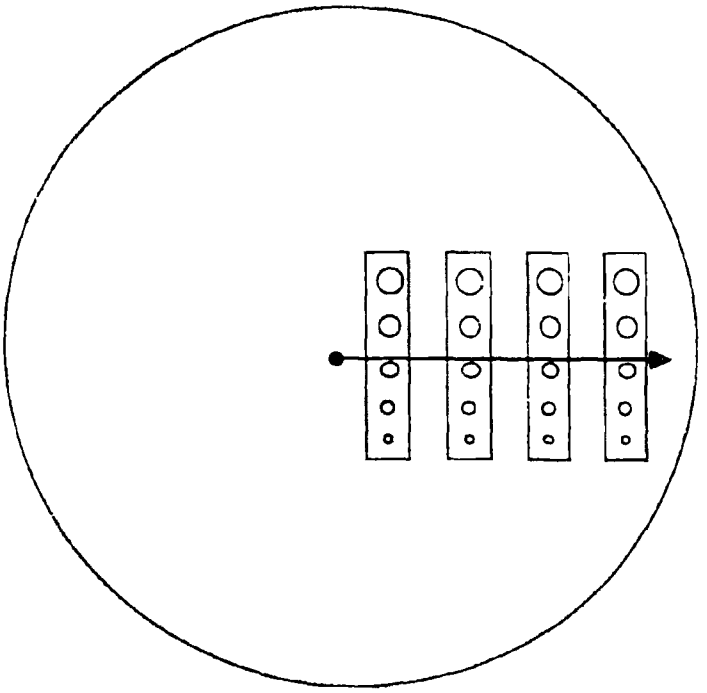

Figure II.E-2. Proposed Method for Incorporation of Single Particle Model into Fixed-Bed Reactor Model Using Five Representative Particle Sizes at Four Representative Particle Locations.

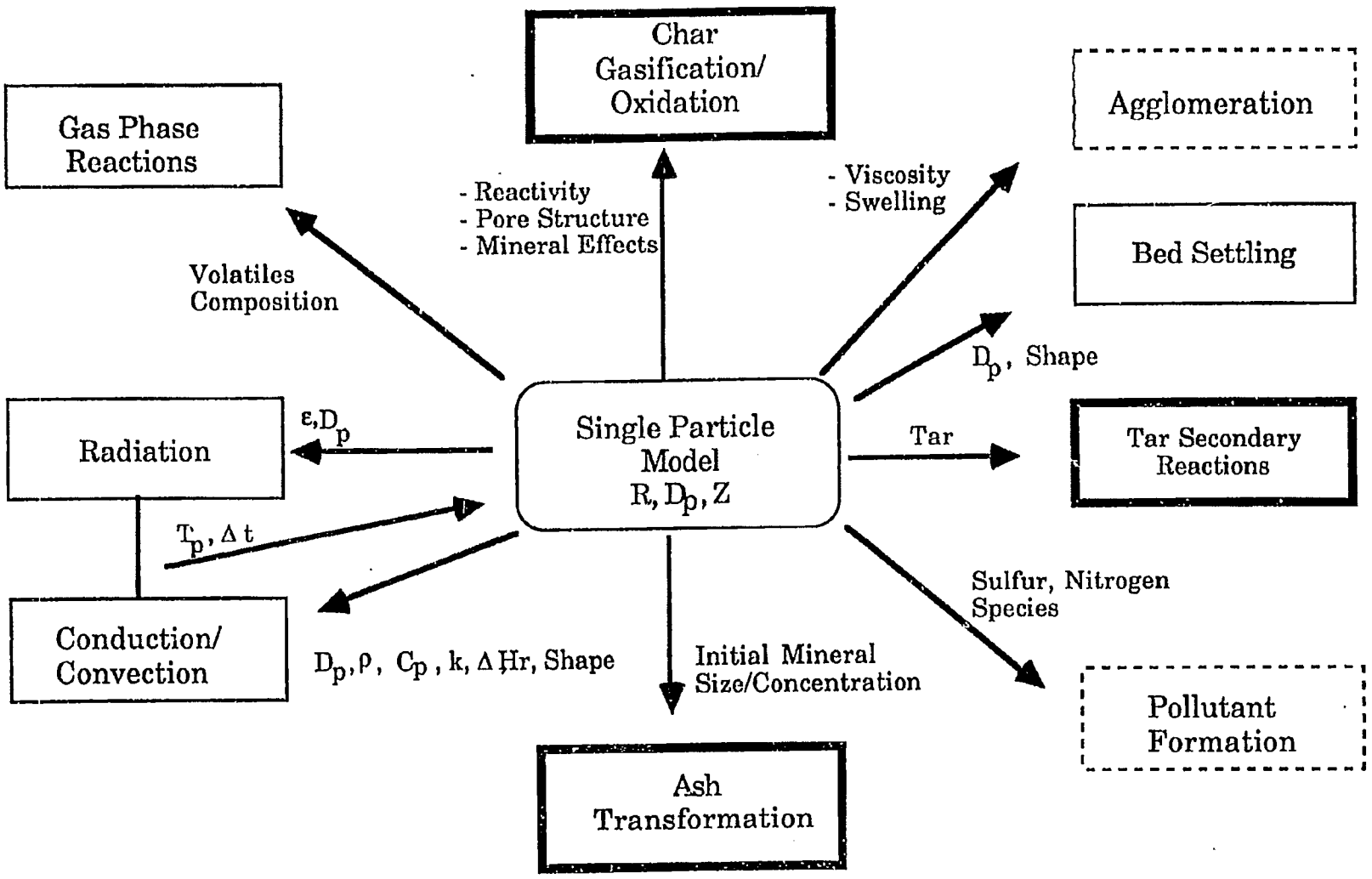

Figure II.E-3. Interface Between AFR Single Particle Model and BYU Advanced Fixed-Bed Reactor Model.

surrounded by bold or dashed lines. The former will be joint development efforts, while the latter fall into the same category but may not be included due to limitations on available resources.

Plans

Complete testing of fixed-bed reactor. Begin model development for large particle submodel. Continue work with BYU on interface of this model with the BYU fixed-bed model. Consider the specific needs for modeling mild gasification processes.

II.F. SUBTASK 2.F. - LARGE PARTICLE OXIDATION AT HIGH PRESSURES

Senior Investigator - Angus U. Blackham
Brigham Young University
Provo, UT 84602
(801) 378-2355

Objectives

The objective of this subtask is to provide data for the reaction rates of large char particles of interest to fixed-bed coal gasification systems operating at pressure.

Accomplishments

Work on this subtask is planned to be accomplished under a single component: High-pressure, large-particle reactor design, fabrication and preliminary data. This subtask is not scheduled to start until the third year.

Plans

This subtask was originally scheduled to start at the beginning of the third year. The original plans called for a literature search to be conducted during the next quarter on large particle char oxidation. During the remainder of the third year, a reactor was to have been designed and constructed. At the present rate of funding of the overall project (lower than originally scheduled), this subtask cannot be initiated during the coming year. However, if the funding is increased to the original schedule, the subtask will be initiated.

II.G. SUBTASK 2.G. - SO_x/NO_x SUBMODEL DEVELOPMENT

Senior Investigators - L. Douglas Smoot and B. Scott Brewster
Brigham Young University
Provo, Utah 84602
(801) 378-4326 and 6240

Graduate Research Assistant - Richard Boardman

Objectives

The objectives of this subtask are 1) to extend an existing pollutant submodel in PCGC-2 for predicting NO_x formation and destruction to include thermal NO, 2) to extend the submodel to include SO_x reactions and SO_x-sorbent reactions (effects of SO_3 in the gas phase will be considered), and 3) to consider the effects of fuel-rich conditions and high-pressure on sulfur and nitrogen chemistry in pulverized-fuel systems.

Accomplishments

Work on this subtask is being accomplished under three components: 1) Extension of the pollutant submodel in PCGC-2 to high pressure and fuel-rich systems, 2) extension of PCGC-2 to allow the injection of sorbent and its reactions in high-pressure, fuel-rich systems, and 3) the formation of sulfur species in the gas phase. Progress during the last year on each of these subtask components is described below.

Component 1 - NO_x at High-Pressure/Fuel-Rich Conditions

The goal of this subtask component is to extend the current pollutant submodel in the comprehensive code to be applicable to high-pressure, fuel-rich conditions such as are common in gasification processes. An important part of this extension is the inclusion of thermal NO formation which may be significant at the higher temperatures typical of gasification in oxygen.

Incorporation of Thermal NO - Kinetic rate equations for thermal NO formation in both fuel-lean and fuel-rich systems were developed from the literature (Zeldovich, 1947; Baulch et al., 1969; Sawyer, 1981). In fuel-lean systems, the following rate expression applies:

$$\frac{\partial X_{NO}}{\partial t} = \frac{9.91 \times 10^{15} K \times sec^{-1}}{T} \exp\left[\frac{-68{,}500}{T}\right] X_{N_2} X_{O_2}^{1/2} P^{1/2} \qquad \text{(II.G-1)}$$

This equation is based on the well-accepted Zeldovich mechanism and assumes oxygen radicals in equilibrium concentration and the concentration of NO to be small. For fuel-rich conditions, the measured rates are often much greater than predicted by this equation. Allowing for oxygen radicals in excess of equilibrium (Sarofim and Pohl, 1973), the following expression results:

$$\frac{\partial X_{NO}}{\partial t} = \frac{4.09 \times 10^{11} K \times sec^{-1}}{T} \exp\left[\frac{-34,900}{T}\right] X_{N_2} X_{O_2} X_{CO} X_{CO_2}^{-1} \qquad \text{(II.G-2)}$$

Under highly fuel-rich circumstances (equivalence ratio > 1.15), the additional elementary reaction

$$N + OH \rightarrow NO + H \qquad \text{(II.G-3)}$$

should be added to the Zeldovich mechanism. Including both the forward and reverse steps of each elementary step results in the following expression (Westenberg et al., 1971):

$$\frac{\partial Y}{\partial t} = \frac{M}{2}\left[\frac{1 - Y^2}{1 + CY}\right] \qquad \text{(II.G-4)}$$

where

$$Y = \frac{[NO]}{[NO]_{eq}} \qquad \text{(II.G-5)}$$

$$M = \frac{5.4 \times 10^{15} K \times sec^{-1}}{T} \exp\left[\frac{-34,900}{T}\right] X_{N_2}^{1/2} P^{1/2} \qquad \text{(II.G-6)}$$

and

$$C = \frac{k_{-2} K_{NO} [N_2]^{1/2}}{k_3 [O_2]_{eq}^{1/2}\left[\frac{1 + k_4 [OH]_{eq}}{k_3 [O_2]_{eq}}\right]} \qquad \text{(II.G-7)}$$

The existing NO_x submodel of PCGC-2 has been revised to allow for any of these three options to be selected.

One challenge seems to be the ability to estimate a priori the non-equilibrium radicals (O, H, and OH) appearing in the thermal NO rate equations. The so-called "partial equilibrium" relationships have been shown to provide a reasonable approach to predict these radical species. Equation II.G-2 used by Sarofim and Pohl (1973) was derived by invoking the partial equilibrium assumption. Another challenge to modeling finite kinetics is adequately describing the chemistry/turbulence interactions. The current approach used in the NO_x submodel of using an assumed probability density function to account for fluctuating species concentration remains the approach of choice at the present time although advances in this area are being made (e.g. Chen and Kollmann, 1988).

NO_x Submodel Evaluation - The BYU entrained-flow gasifier was simulated with PCGC-2 to evaluate the combined thermal NO and fuel NO submodel for fuel-rich combustion. The case examined was for Utah Bituminous coal gasified at a stoichiometric ratio of -0.4 (Brown et al., 1986). Equation II.G-1 was used for this simulation. Joint prediction of fuel and thermal NO increased the peak NO value by approximately 25% over the value predicted by fuel NO alone. Figure II.G-1 compares the reactor centerline prediction with centerline measurements. The addition of thermal NO to the model improves the model predictions along the entire profile. Additional details about this case are discussed in the 7th Quarterly Progress Report (Solomon et al., 1988).

In order to more thoroughly evaluate the mechanism for thermal NO in the NO_x model, it is desirable to make comparisons between predicted and experimental NO concentrations in gaseous, fuel-nitrogen-free, combustion systems. A literature survey of experimental thermal NO investigations was described in the 5th Quarterly Progress Report (Solomon et al., 1987). The vast majority of the available data are reported for bench-scale reactors with unique reactor geometry and flow conditions. PCGC-2 is currently applicable to fully turbulent, axi-symmetric flow reactors. Detailed profiles of the temperature, major species, and NO concentrations are also necessary to confidently make an evaluation of the model performance. None of the data located from previous studies were judged to be completely suitable according to these criteria. The experimental investigation of Takagi et al. (1981) of a turbulent-jet propane fuel and laminar co-flowing air stream was selected for model prediction since major species, pollutant, and temperature profiles, although limited, were reported as well as adequate information to simulate this reactor. A reactor schematic was shown in the 7th Quarterly Report (Solomon et al., 1987). The major limitation of this case is the inability of PCGC-2 to accurately model the mixing of the laminar air stream with the turbulent fuel jet. This experimental investigation, however, is not unlike many other studies in which a similar laboratory burner was used.

The results of this simulation were also presented in the 7th Quarterly Report. Rate expressions given in Eqs. II.G-1 and II.G-2 were investigated for this case with little difference in the predicted results. Figure II.G-2 shows a comparison of the data with model predictions for thermal NO. In this plot, an axial location of 150 mm for predictions is compared with data measured at 200 mm in order to match temperature profiles, since temperature is one governing parameter of the thermal NO rate expression. Although the NO_x submodel accurately predicted the measured NO profile early in the reactor, the predicted effluent NO concentration was substantially higher than was measured. This discrepancy is attributed to neglect of the reverse rates of the individual

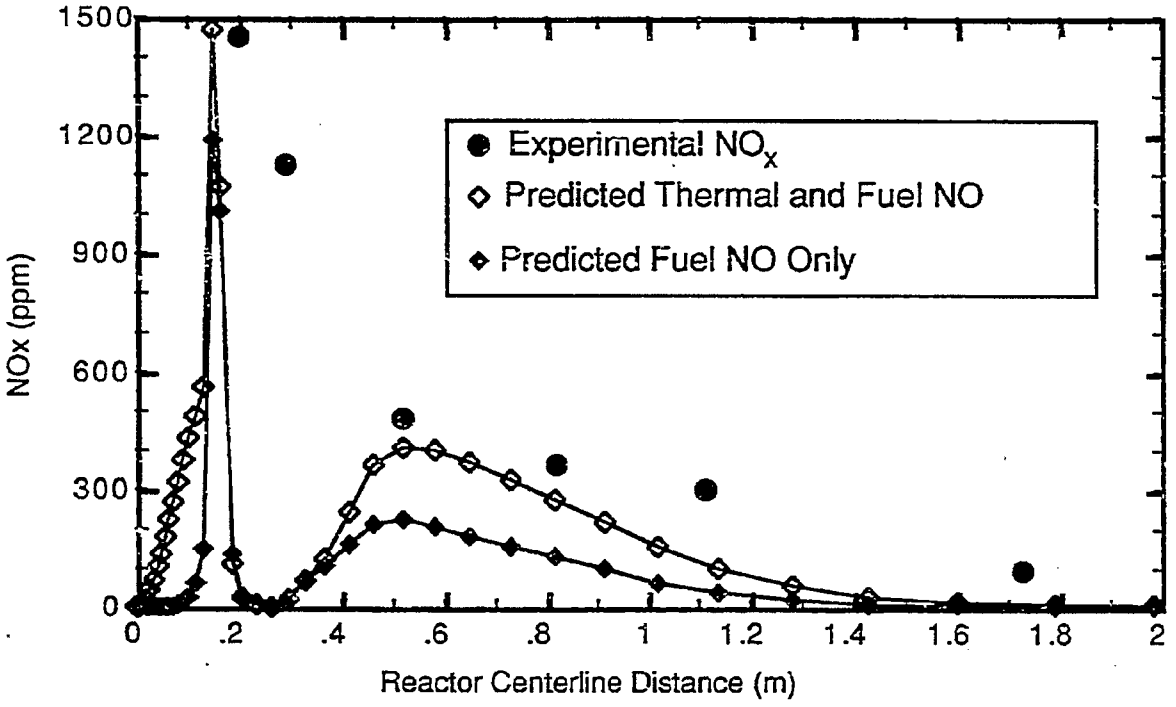

Figure II.G-1 Comparison of centerline NOx profiles for the gasification of Utah bituminous coal (data of Brown et al., 1986)

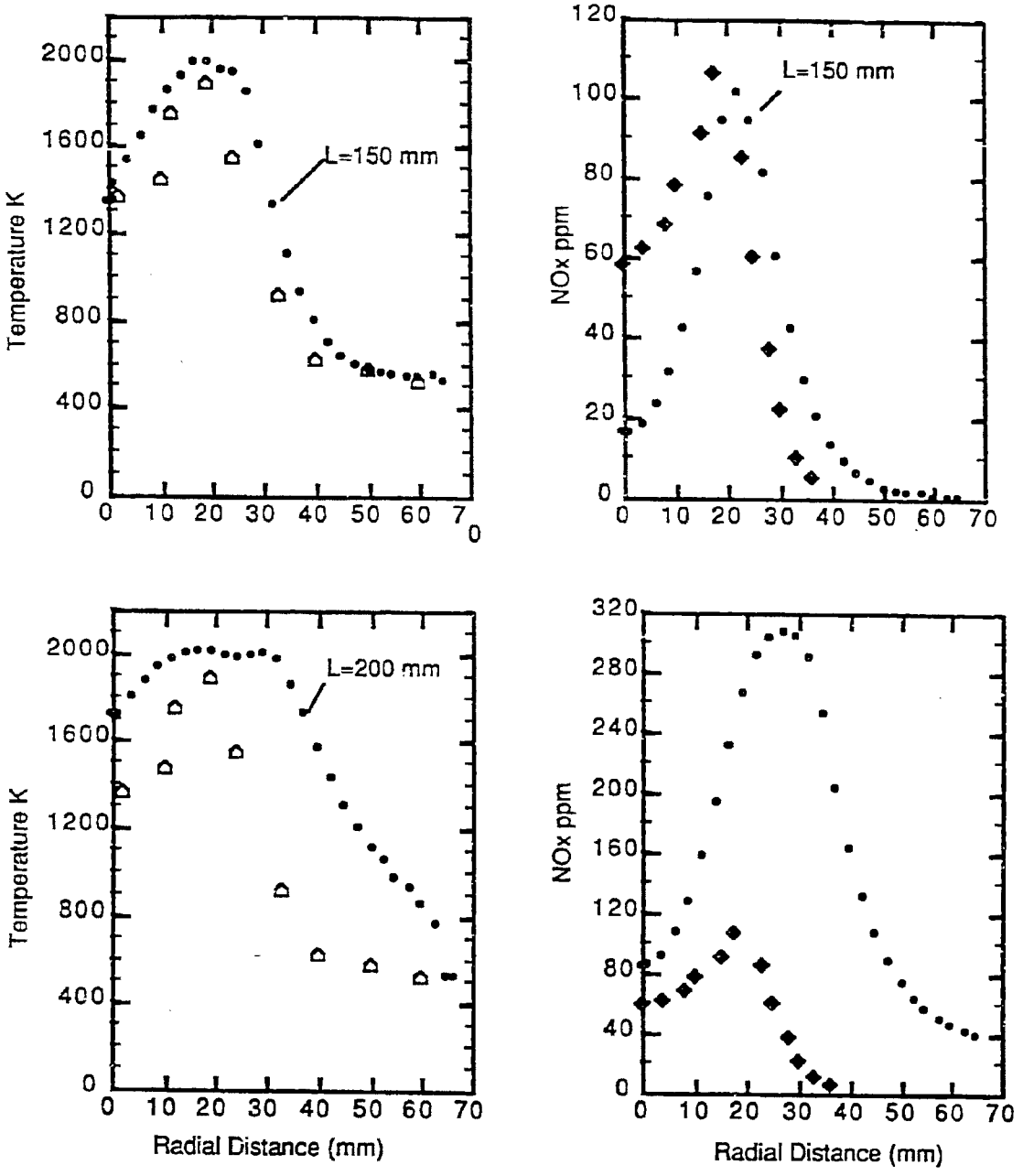

Figure II.G-2. Comparison of experimental and predicted radial profiles for propane/coflowing air combustion. Predicted profiles of L = 150 mm and L = 200 mm are compared to the data (Takagi et al., 1981) measured at L = 200mm. Symbols - data Dots - predicted quantities.

elementary steps used in deriving Eqs. II.G-1 and II.G-2. This is approximately true only when the concentration of NO is low but fails when NO concentrations are significant as they likely are in the aft section of the combustion tube. Equation II.G-3 does not require this assumption and will next be invoked and tested in the submodel to verify the above explanation.

Due to the lack of suitable data in the open literature for rigorous NO_x model evaluation, a test program is being designed for measuring both thermal NO and fuel NO in gaseous and coal-laden flames using an advanced reactor currently under construction at BYU under independent funding (Eatough, 1988). This reactor will simulate heating rates and temperatures typical of industrial boilers. Emphasis has been placed on measuring the temperature and species concentrations. The data collected in these tests can be used to evaluate the thermal NO mechanism in the NO_x submodel as well as the joint formation of fuel and thermal NO.

Component 2 - Sorbent Particle Chemistry

This subtask component is aimed at developing a sorbent particle submodel for incorporation into PCGC-2. The submodel will include both calcination chemistry and reactions with the gas phase. The submodel will be an extension of independent work being performed by Pershing and coworkers at The University of Utah, where a sorbent chemistry submodel for fuel-lean conditions is being developed and incorporated into PCGC-2. Modification to the code have been made to track the sorbent particles through the reactor (Wormeck, 1988), also under independent funding. A grain-model which predicts the capture of SO_2 by CaO is being integrated into the code and is approaching completion.

The reaction model of SO_2 capture was developed and evaluated by Silcox (1985). Briefly the model accounts for diffusion from the bulk gas to the particle's surface, pore diffusion to the particle's interior, solid-state diffusion through the product layer, and reaction at the product-CaO interface. The stoichiometric reaction is written as follows:

$$CaO + SO_2 + {}^1/_2\, O_2 \rightarrow CaSO_4 \qquad \text{(II.G-7)}$$

The integration of the sorbent particle reaction submodel will be completed during the coming year. Details that remain to be completed include consideration of a mechanism for H_2S capture (i.e. fuel-rich conditions). A task was initiated to investigate incorporating a separate reaction model to account for H_2S capture, providing a complete model for both fuel-rich and fuel-lean combustion systems. Efforts are being made at BYU to facilitate the model integration and provide the final submodel product.

Component 3 - SO_x Formation

This subtask component will model the gas-phase reactions that generate the sulfur species for input to the sorbent capture model developed under Component 2 of this subtask. A review of the literature is being made to identify recent work related to sulfur pollutants. Objectives include: 1) identifying the steps in the SO_x formation process, 2) isolating the most

important or rate-determining steps, 3) identifying the dominant products or stable species in combustion gases, 4) determining whether an equilibrium approach is acceptable, 5) gaining an understanding of the effect of reactor parameters and operating conditions on the sulfur species, and 6) identifying important SO_x/NO_x interactions.

SO_x Submodel Development - A review of recently published literature regarding sulfur pyrolysis from coal and gas phase conversion to sulfur species has been completed. A summary of the key findings was discussed in the 7th Quarterly Report (Solomon et al., 1988). The following aspects have been identified as important to the predictive method. Each of these aspects involves complex mechanisms which are not completely certain.

1. The physical and chemical transformation of sulfur constituents in the coal during pyrolysis.

2. Chemical conversion of the devolatilized sulfur species to stable species via homogeneous and heterogeneous reactions.

3. Secondary NO_x/SO_x and alkaline metal interactions.

Neither the necessity nor the feasibility a detailed kinetic model have yet been determined. These questions will be addressed in the third year. First, the submodel will be evaluated using data collected under Subtask 2.h and other data from the BYU gasifier (Highsmith, 1982; and Nichols, 1985). Gas phase equilibrium will be assumed for the sulfur species. The rate of sulfur release will be assumed to be proportional to the total coal mass loss. From this evaluation, insight will be gained to determine if equilibrium chemistry will suitably predict the sulfur species pool.

If the equilibrium assumption is not acceptable for predicting SO_2, H_2S, and COS, then a well-designed global mechanism should be developed and employed. The chemistry of sulfur in flames has received considerable attention, as shown by Cullis and Mulcahy (1972), who reviewed over 400 papers published by the early 1970's. In more recent years, some of the key studies of fuel-sulfur reaction have been made by Kramlich (1981), Solomon (1977), Highsmith (1982), Zaugg (1984), and Nichols (1985). Zaugg (1984) presents and discusses the feasibility of describing the reaction paths shown in Figure II.G-3 and suggests some simplifications for arriving at a tractable global kinetic model.

Until recently, very few correlations between the sulfur in coal and its distribution in the products and evolution rates have been available. Separate investigations are in progress to correlate the influence of coal type (i.e., total coal-bound sulfur and/or sulfur forms) with the distribution among solid (char) liquid (tar) and gaseous phases during devolatilization (Khan, 1988; Fatemi-Badi et al., 1988; Oh et al., 1988). The yields of these phases and the distribution of early volatiles between H_2S and COS have been observed and fit to various models.

Submodel Evaluation NO_x/SO_x Coupled Effects - Evaluation of the SO_x submodel will include comparison of experimental data from three separate investigations of sulfur pollutant formation from coal conversion processes to PCGC-2 simulations with equilibrium calculation of the sulfur species. The first experimental study that will be simulated is for detailed local pollutant

measurements in an entrained coal gasifier (Highsmith, 1982). This work was continued by Zaugg (1984) for fuel-lean combustion of coal. Finally, the recent measurements of Hedman and coworkers of sulfur species formation and capture by injected sorbents under Subtask 2.h will be used to evaluate the modelling approach.

Verification of the sorbent-particle reaction submodel will be made jointly by The University of Utah and BYU during the upcoming year. The gasifier data obtained under Subtask 2.h will again be utilized in this evaluation.

Plans

During the first quarter of the third year, the data collection task will be completed. This will be done in coordination with Eatough and coworkers during the start-up of the BYU-ACERC reactor. Concurrent with this effort, additional data from the open literature will be sought from Leukel and coworkers at the University of Karlsruhe and any other sources that become available. Following this data procurement, the thermal NO mechanism will be evaluated. This evaluation should be completed by the end of the second quarter. Evaluation of the combined fuel and thermal NO model will also continue.

Model simulation will be made during the first two quarters to determine the validity of predicting the gaseous sulfur chemistry using an equilibrium approach. The sorbent-particles reaction submodel will be completed in the upcoming quarter and an evaluation of the model will begin. This evaluation will be completed during the second quarter. The combined SO_x/sorbent-reaction-model will then be jointly tested.

II.H. SUBTASK 2.H. - SO_x/NO_x SUBMODEL EVALUATION

Senior Investigator - Paul O. Hedman
Brigham Young University
Provo, UT 84602
(801) 378-6238

Student Research Assistants - David Braithwaite, Aaron Huber,
Laren Huntsman, and Gregg Shipp

Objectives

The objectives of this subtask are 1) to obtain detailed profile measurements for radial crossjet injection of sorbent particles in a cold-flow facility designed to replicate the geometry of a 2-D combustor/gasifier, 2) to obtain concentration profile data for sulfur and nitrogen pollutant species from laboratory-scale, coal reaction tests at atmospheric and elevated pressure with and without sorbents, and 3) to investigate the effect of pressure on the effectiveness of sorbent injection in capturing sulfur pollutants. These data are to be used to characterize sorbent flow and sulfur capture and for sorbent submodel evaluation.

Accomplishments

This subtask is being carried out under three subtask components: 1) a cold-flow investigation of sorbent-mixing fluid mechanics, 2) modifications of the laboratory-scale reactor to accommodate sorbent particle injection, and 3) space-resolved sulfur and nitrogen pollutant measurements in the laboratory-scale reactor.

Component 1 - Sorbent Mixing Fluid Mechanics

This subtask component is aimed at 1) obtaining detailed profile measurements for radial crossjet injection of sorbent particles in a cold flow facility designed to replicate the geometry of a 2-D combustor/gasifier; and 2) identifying flow parameters which will lead to rapid mixing of sorbent particles with the free stream flow.

The BYU cold-flow facility has been used to simulate the flows that exist in the entrained-flow gasifier when sorbent is injected into a flow that is perpendicular to the main gasifier flow. Previous investigators (see Webb and Hedman, 1982; Jones et al., 1984; and Lindsay et al., 1986) have used the BYU cold-flow facility to simulate the flows that exist in one of the BYU coal combustors and the BYU entrained-flow gasifier. The existing cold-flow facility has been modified to include crossflow jets for sorbent injection. Also, the flow chamber design was also changed from previous studies. The new flow chamber has been made of transparent plastic to simplify making LDA measurements and enable qualitative flow visualization with smoke.

During the report period, the design of a cold-flow experiment to simulate the injection of sorbent particles in an entrained-flow coal reactor was completed. Tests were performed in a transparent, cylindrical flow chamber with crossflow jet injection. A flow straightener was added to the apparatus so that the free stream flow would be fully developed in the mixing region.

Three testing techniques were used for this study. First, smoke injection for flow visualization was used to obtain qualitative information of the trajectory and mixing patterns of the crossflow injectors. Second, trace gas was injected in crossflow, and gas extractions were taken at different locations in the flow chamber. Analysis of the gas samples provided quantitative data on the mixing of the two streams. And third, laser Doppler anemometer (LDA) data were taken to determine the velocity and turbulence characteristics of the flows.

Smoke injection was accomplished by dripping an ethylene-glycol-based fluid into an externally heated pipe. The fluid vaporized to produce a highly visible white smoke. The smoke was entrained in air and carried into the mixing chamber. Photographs were taken of smoke injected at different flow rates and with various injector sizes to illustrate the jet trajectories.

Trace gas injection tests used carbon dioxide injected in crossflow. Gas samples were taken through a system of probes. A rigid fastener was employed to fix the position of the probes in the flow. Unused probes recessed into the flow chamber walls in order to minimize flow disturbances. Gas samples were obtained on a Cartesian grid of 45 data points at 4 different axial locations downstream from the crossflow injectors. An on-line, infrared analyzer was used to determine the CO_2 concentration in the gas samples. Contour maps were prepared from these data, using linear interpolation between data points and a weighted cubic spline technique to generate contour lines.

Laser Doppler anemometer measurements provided a means of obtaining non-intrusive velocity data with a high degree of accuracy. LDA measurements were made using a 100 mW argon-ion laser with TSI brand optics and signal processors. Axial velocity measurements were taken on a horizontal plane at the mixing chamber centerline. Typically, 1000 Doppler bursts were used to determine the average and rms velocity at a point in the flow. Since LDA systems require the presence of small particles in the flow to determine velocity, fluidized-bed feeders with micron-sized alumina particles were used to seed the flow. Frequency shifting and time-weighted averaging were employed to reduce LDA bias effects.

Testing for the cold flow portion of this study has been completed, and analysis of the test results is nearly completed. The results are discussed below.

<u>Flow Visualization Results</u> - Photographs of smoke injected into the flow chamber at different momentum ratios [J represents the ratio of the momentum flux in the jet $(\rho u^2)_{jet}$ to the momentum flux in the duct $(\rho u^2)_{duct}$] are shown in Figure II.H-1. The pictures illustrate the deflection of the jet plume which took place as it was entrained in the free stream. The bending of the jets occurred as a result of momentum exchange, with the free-stream fluid deflecting the jets in the chamber axial direction. The top photograph illustrates the flow patterns for a jet with a relatively low momentum ratio (J=10, d_j=1.04 cm). The crossflow jet penetrated only moderately into the duct before it was swept in the chamber axial direction by the free stream. The jet and free-stream fluids mixed locally, but the jet stayed relatively isolated from a large portion of the main flow. Ferrell et al. (1985) reported that at a crossflow-to-free-stream velocity ratio of 2, the lateral injection had an effect on only

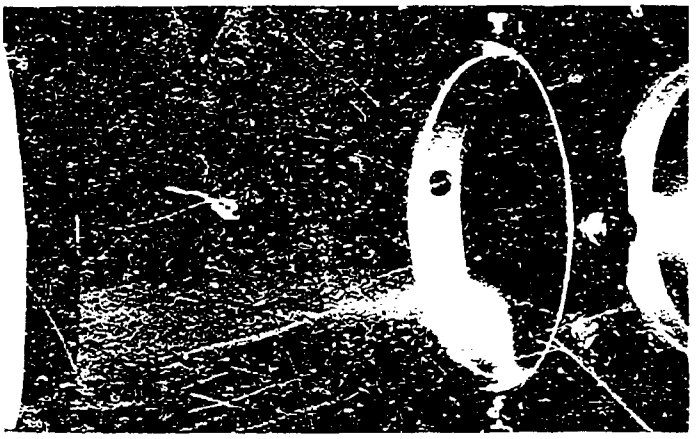

J=10, dj=1.04 cm, Re=3000

J=50, dj=1.04 cm, Re=3000

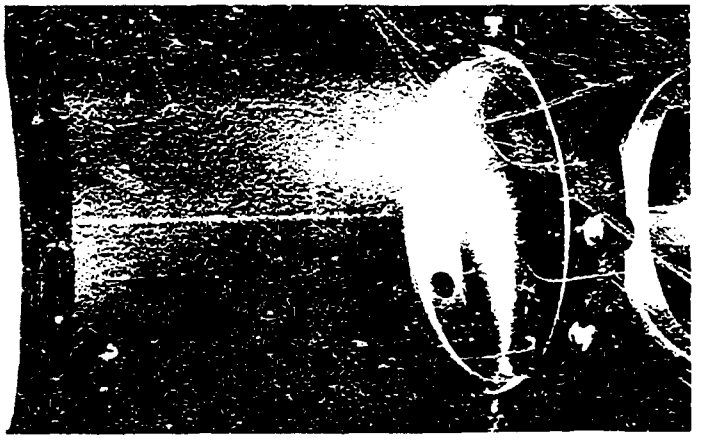

J=90, dj=1.04 cm, Re=3000

Figure II.H-1. Photographs showing the effect of jet to free stream momentum ratio on jet trajectory.

the half of the flow chamber closest to the injection port. These flow visualization tests tend to confirm that observation.

At a higher momentum ratio (J=50, d_j=1.04 cm), as shown in the center photograph, the jet penetrated to about the centerline of the flow chamber. This increased penetration caused the jet to interact with a greater portion of the free-stream fluid, improving the overall mixing rate.

At an even greater value of momentum ratio (J=90, d_j=1.04 cm), as shown in the bottom photograph, the jet had sufficient energy to impinge on the opposing wall before being entrained in the free-stream flow. The jet was broken up at the wall and mixing was further enhanced by this dispersion of the jet fluid. This photograph also shows a small recirculation zone which formed just upstream from the point where the jet plume impinged on the duct wall. This recirculation zone formed as a result of the jet fluid being scattered tangentially after hitting the wall.

The effect of jet diameter (d_j) at about constant mass flow rate on penetration is illustrated in Figure II.H-2. In the top photograph the jet diameter is 0.48 cm, while in the middle and bottom pictures the diameters are 0.71 and 1.04 cm, respectively. Penetration of the jet into the duct is roughly the same in all the cases shown, but the momentum ratios range from 225 down to 75. This suggests that a smaller jet bends more quickly at a given momentum ratio than a larger one.

An analogy can be drawn between a jet in crossflow and a mechanical component under some load. Both size and stiffness of the component effect its deflection. In the situation under consideration, the jet momentum can be thought of as the stiffness of the jet, while the diameter also plays a part in how easily the jet can be turned by the free-stream flow. These two parameters are somewhat coupled since, for a given mass flowrate, jet momentum is a function of diameter.

Several previous researchers have developed empirical correlations to describe the centerline trajectory of a jet injected normal to another flow. Cetegen et al. (1987) performed a detailed analysis of the correlations developed by 7 different studies and arrived at this overall average:

$$\frac{y}{d_j} = J^{0.43}\left[\frac{x}{d_j}\right]^{0.36} \qquad \text{(II.H-1)}$$

where x and y represent the chamber axial and radial distance, referenced from the injection point, d_j is the jet diameter, and J is the jet-to-free-stream momentum ratio. This correlation allows jet trajectory to be determined similarly for any jet diameter in an unbounded main flow. Although it is difficult to ascertain the centerline location of a deflected turbulent jet, the trajectory of the smoke traces shown here are in qualitative agreement with this empirical correlation. This indicates that in a bounded flow the opposing wall has little influence on jet trajectory unless the jet has sufficient energy to impinge upon it. Kamotani and Gerber (1974) also observed that the

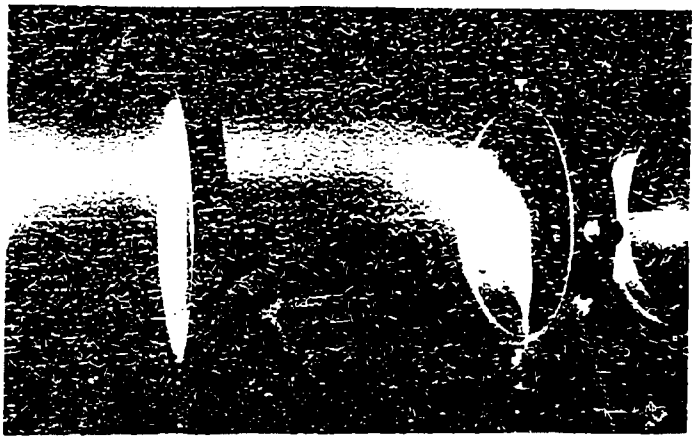

J=225, dj=0.48 cm, Re=3000

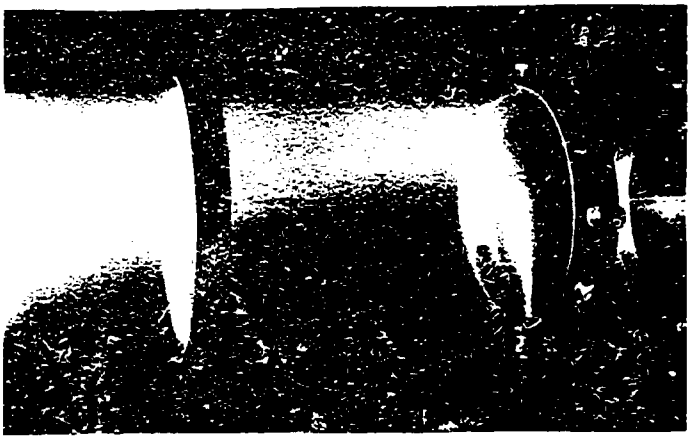

J=120, dj=0.71 cm, Re=3000

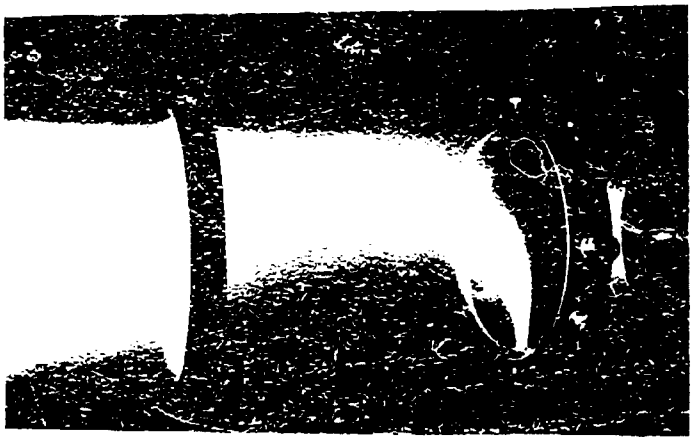

J=75, dj=1.04 cm, Re=3000

Figure II.H-2. Photographs showing the effect of injector diameter on jet trajectory.

influence of confining walls was minimal for crossflow jets with insufficient energy to penetrate the entire width of the flow chamber.

Mapping of Trace Gas Data - Contour maps of trace gas mass fraction, normalized by the well-mixed trace gas mass fraction, are presented to quantify the mixing patterns of the cross-flow jets. Normalizing with this method allows the relative stoichiometry of the flow chamber to be visualized. Since the tracer gas is used to represent sorbent injection, at a specific value of overall sorbent-to-sulfur ratio, the unity contour represents the duct location where that specific sorbent-to-sulfur ratio is achieved. A contour of 2 represents the duct location where twice the specific value exists. A contour of 0.5 represents a duct location where the specific sorbent-to-sulfur ratio is one-half of the specified value, and so on.

Figure II.H-3 shows the flow patterns associated with a single crossflow injector at four axial locations. The jet-to-free-stream momentum ratio was approximately 575 and jet diameter was 0.71 cm. This momentum ratio was sufficient to cause the jet to impinge on the opposite wall of the flow chamber. Upon hitting the opposite wall, the jet fluid spread out along the duct walls, and caused regions of high trace gas concentration at the lower part of the chamber circumference. As the flow moved downstream, the jet and free-stream fluids mixed through turbulent diffusion, and the mass fraction gradients became less steep.

The mixing patterns for 3 jets spaced 120 degrees apart along the duct circumference are shown in Figure II.H-4. The total volumetric jet flowrate was the same as that shown for a single jet, but in this case the flow was spread out over 3 injectors. The momentum ratio was therefore reduced, and with it the jet penetration. However, the jets did have enough momentum to penetrate to the center of the mixing chamber and interact with each other. The majority of the jet fluid was located in a circular region near the centerline, indicating that the jets had impinged on each other. This circular pattern of jet fluid was characteristic of all flow cases employing multiple opposing injectors, with the jets having sufficient energy to penetrate to the duct centerline. The total penetration of the jets was curtailed by interaction with the opposing flows. Mass fraction gradients were steep in the region of the injection points, and the trace gas became less locally concentrated at downstream locations as the flows mixed. Rathgerber and Becker (1977) observed that the far downstream flowfield for a jet in crossflow was dominated by dispersion due to pipe-flow turbulence. The mapping data in this study agree that as distance increases downstream from the crossflow injectors, the flow structure becomes more typical of pipe flow.

The mixing patterns shown in Figure II.H-4 are not completely symmetric. Fluid from the uppermost injector was dispersed along the jet path, rather than being completely concentrated near the centerline. This was attributed to inequality in the individual jet flowrates, and to imperfections in the injectors which may have caused additional turbulence and increased dispersion of the jet plume.

Tracer gas tests conducted at relatively low jet-to-free-stream momentum ratios confirmed the observation that such flows are slower to mix with the free stream than flows with sufficient energy that they impinge either on an opposing jet or confining surface. In cases employing low momentum ratios, increasing

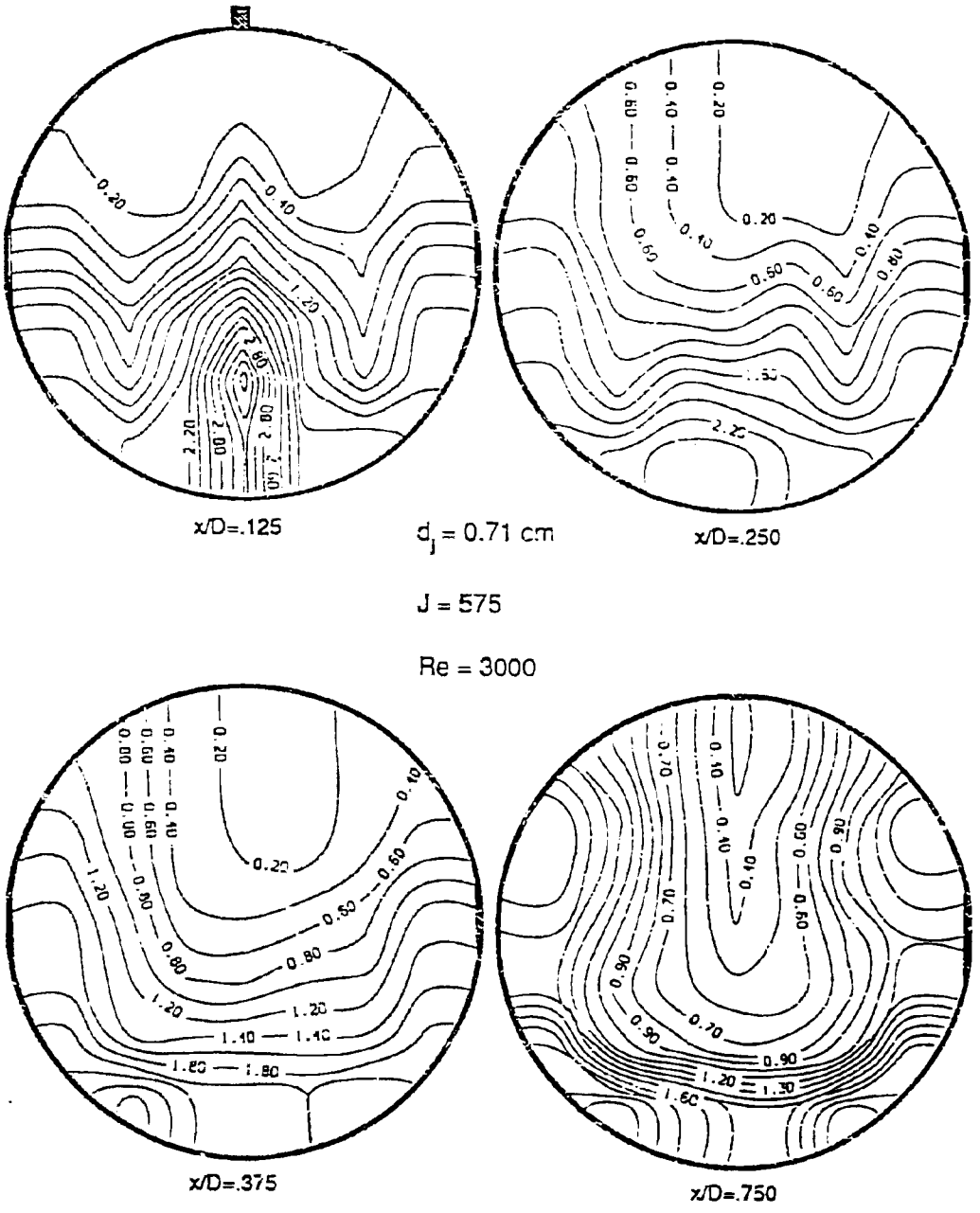

Figure II.H-3. Contours of trace gas mass fraction normalized by the well-mixed mass fraction for a single injector.

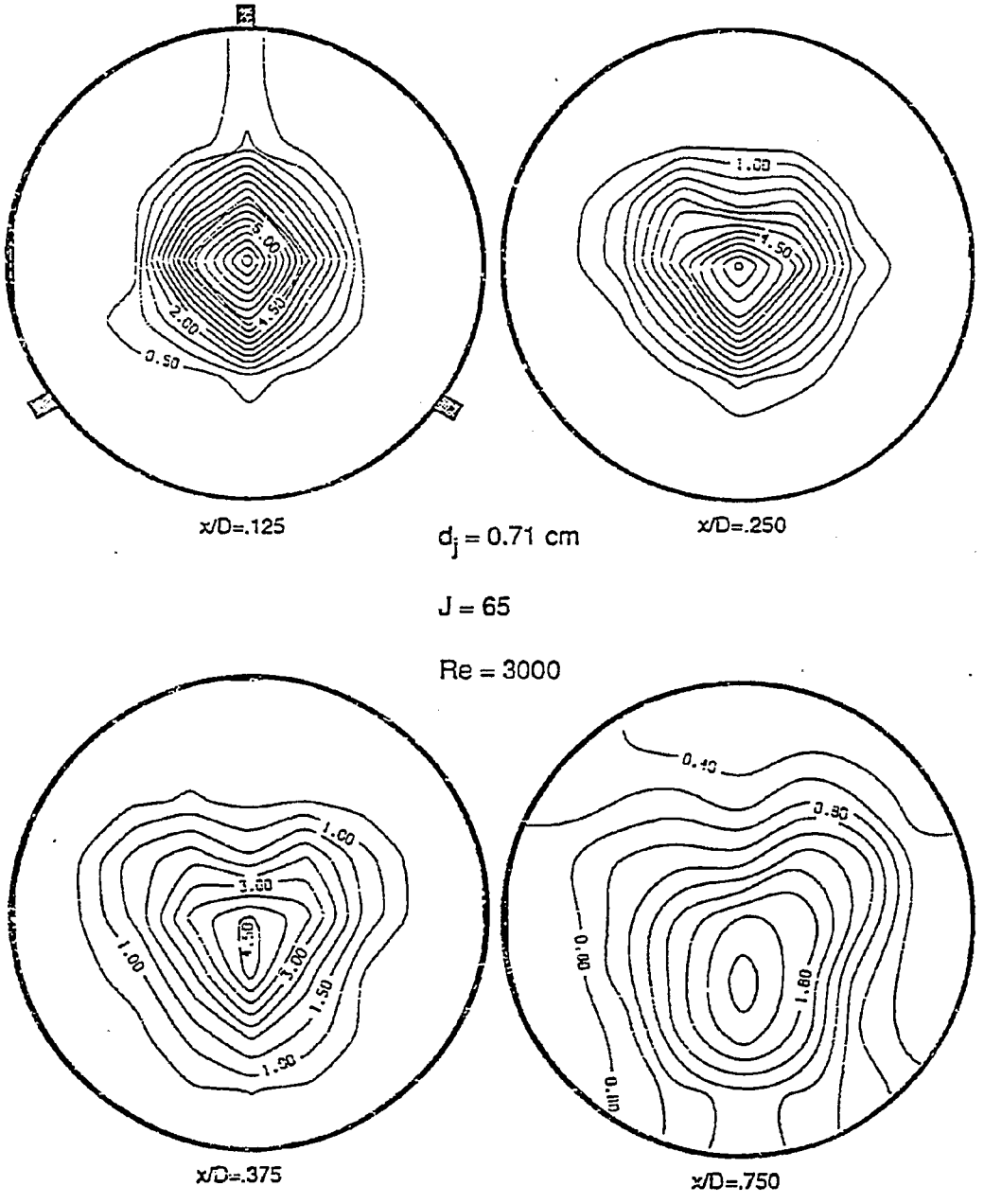

Figure II.H-4. Contours of trace gas mass fraction normalized by the well-mixed mass fraction for three injectors.

the number of crossflow injectors was found to provide improved mixing of the streams since the multiple injectors covered a larger portion of the free-stream cross-section.

An interesting effect associated with free-stream Reynolds number is illustrated in Figure II.H-5. In this case, the free-stream Reynolds number (Re=1500) was typical of laminar flow in a cylindrical chamber. Close to the injection point, the mixing patterns were similar to those seen at higher free-stream Reynolds numbers. However, as the jet fluid moved downstream, buoyancy began to strongly affect the fluid behavior. The CO_2 used as a tracer gas was approximately 1.5 times more dense than air at the same temperature. At x/D = 0.750, the flow was obviously layered with the heavier carbon dioxide sinking to the bottom of the duct.

Observing relatively strong buoyancy forces was somewhat surprising since gravitational effects are often neglected in flows of this type. Holdeman (1983) reports that density effects are of secondary importance when jets are injected in crossflow. Buoyancy effects were observed in all the flow cases conducted with Reynolds numbers in the laminar regime. However, at Reynolds numbers representative of transitional or turbulent flow, buoyancy effects were not detected. The onset of turbulence, with the additional stresses and energy dissipation it brings, disturbs the flow patterns sufficiently that buoyancy effects can properly be neglected in turbulent flow for gases with densities similar to those considered here. However, in laminar flow, even small density gradients can have significant effects on flow behavior. Buoyancy effects have received little treatment in the literature, since most investigations are conducted with turbulent flows.

The fact that buoyancy effects were present reveals that the predominant flow structure, even with crossflow injection, was laminar at low free-stream Reynolds numbers. Although the flow was undoubtedly turbulent very close to the injection ports, it became predominantly laminar again at approximately 1 duct radius downstream from the jets.

Buoyancy effects would be even more pronounced if the flow were actually entraining sorbent particles. Since particle density is many times larger than gas density, the particles would be strongly influenced by gravity at low Reynolds numbers. However, since most pulverized coal reactors are either up-fired or down-fired and generally highly turbulent, buoyancy effects would probably not be a concern when injecting sorbent.

Laser-Doppler Velocity Measurements - LDA data were obtained along a horizontal plane at the main duct centerline. Data were obtained at the free-stream inlet, and also in the mixing region to characterize velocity and turbulence intensity profiles. Inlet information was obtained so that data from this study would be of use in validating comprehensive code predictions.

Velocity profiles measured at the mixing chamber inlet were typical of fully-developed flow in a circular duct. Data taken at Re=1500 showed a classical laminar profile, while data for Re=3000 and Re=4500 showed velocity profiles associated with transitional, and fully turbulent flow respectively.

Figure II.H-6 shows the velocity profiles obtained downstream from the crossflow jets for cases employing 1 and 3 injectors at a free-stream Reynolds

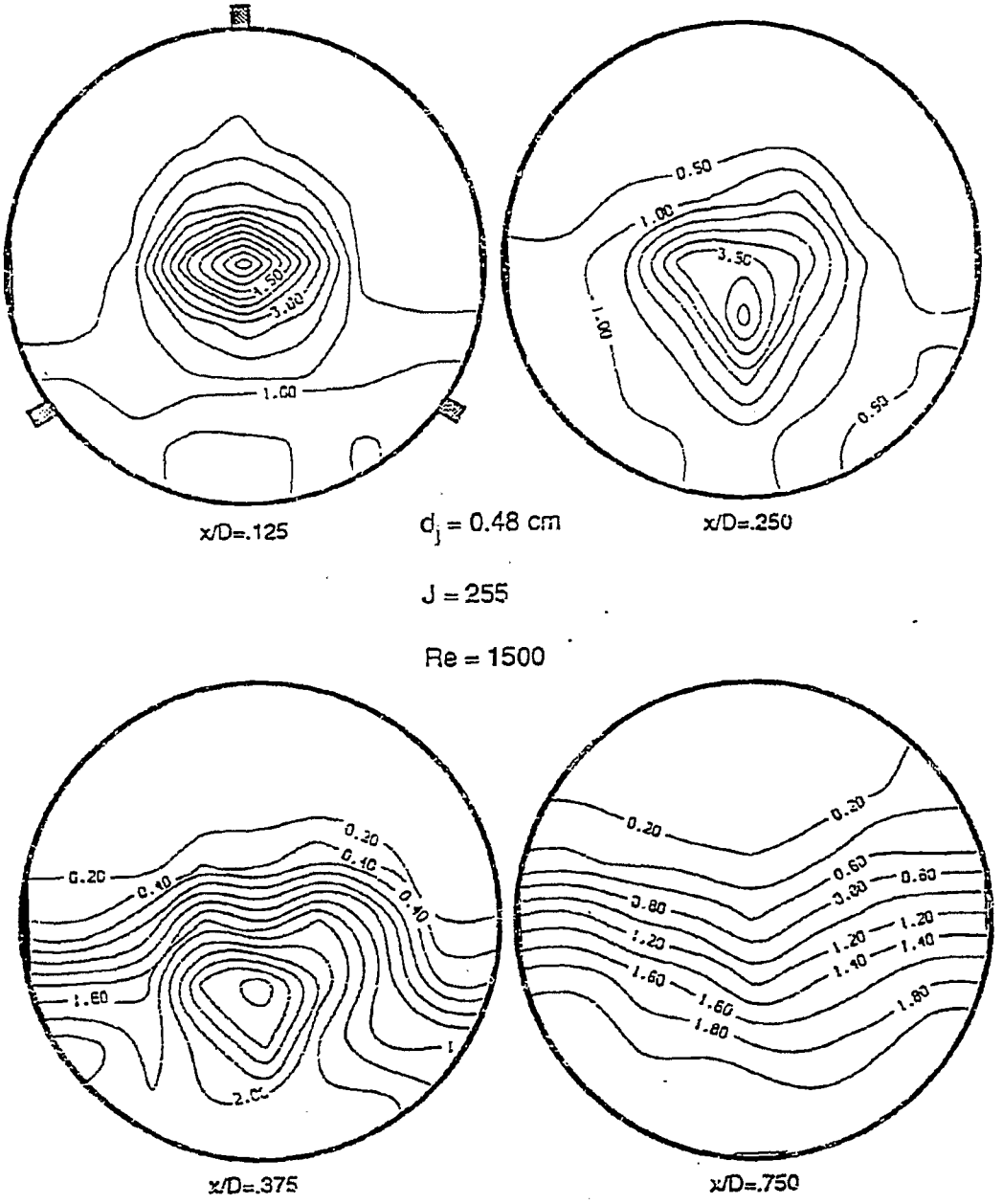

Figure II.H-5. Contours of trace gas mass fraction normalized by the well-mixed mass fraction for three injectors at low free stream Reynolds number.

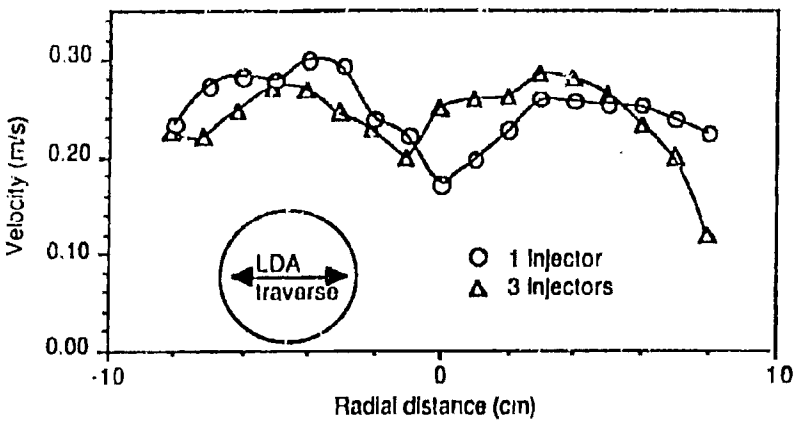

Figure II.H-6. Velocity profiles at x/D =.125, for 1 and 3 injectors.

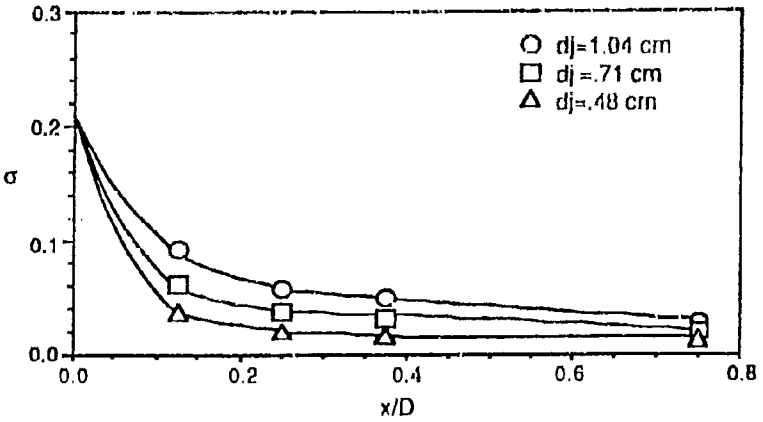

Figure II.H-8. Standard deviation of trace gas mass fraction from the well-mixed mass fraction, at different axial locations for flow cases employing injectors with different diameters.

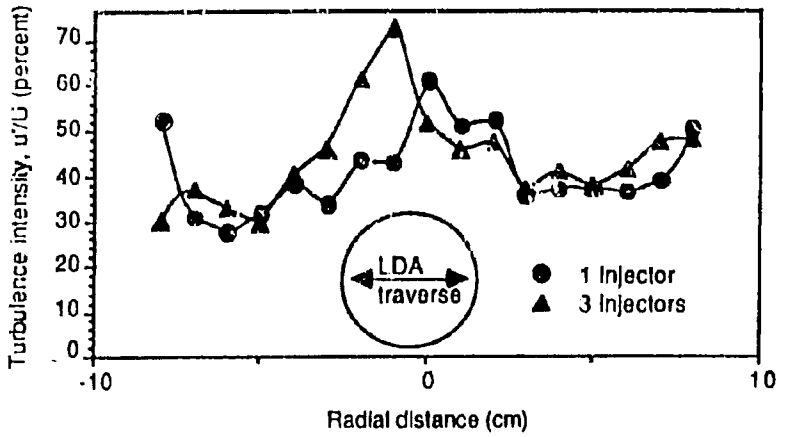

Figure II.H-7. Turbulence intensity at x/D = .125, for 1 and 3 injectors.

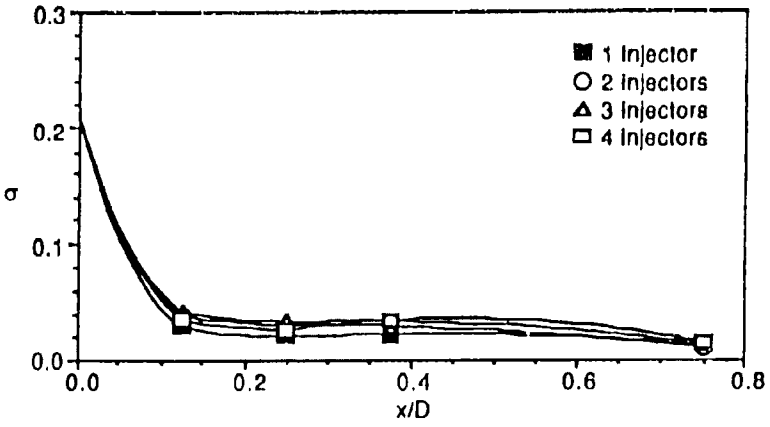

Figure II.H-9. Standard deviation of trace gas mass fraction from the well-mixed mass fraction, at different axial locations for flow cases employing different numbers of injectors.

number of 3000. For a single injector, the velocity slowly increased moving away from the wall; however, within about 2 cm of the duct centerline, the velocity was substantially reduced. With the jet configuration used, the crossflow fluid passed directly through this region of reduced velocity. This would indicate that the jet fluid caused an obstruction in the flow. The free stream fluid was disturbed by the jet and forced around it. Thus, the region of highest axial velocity straddled the duct centerline, where free stream fluid accelerated around the obstruction caused by the crossflow. Comparison of the LDA and tracer gas data for this case reveals that this zone of highest axial velocity was composed almost entirely of fluid from the free stream, with the trace gas being concentrated in surrounding regions.

These same patterns appear in the velocity profiles for the three injector case. There is a region of lower axial velocity, where the injected gases were concentrated, and the velocity went through a maximum in areas not passed through by the jets, where trace gas mass fraction was low. For three injectors, the drop in axial velocity near the walls was more pronounced than for a single jet. Tracer gas data showed that, for a single jet, the jet fluid impinged on the opposing wall and spread along the duct circumference. This spreading caused the flow near the chamber walls to take on a more turbulent character, as jet fluid was entrained in the free stream, while for three injectors, the flow near the chamber walls was relatively undisturbed and retained a velocity profile characteristic of transitional flow.

Figure II.H-7 displays the axial turbulence intensity measurements obtained with the LDA for the flow cases being discussed (Re=3000, 1 and 3 jets). For a single injector, the plot shows that turbulence intensity was highest at the duct centerline and near the chamber walls. Comparison of these data with the velocity profiles and tracer gas maps, reveals that these regions of high turbulence intensity were associated with entrainment of jet fluid in the free steam, while the region of highest axial velocity, where free-stream fluid accelerated around the jet, had a relatively low turbulence intensity. The turbulence intensity data are in agreement with the work of Crabb et al. (1981), who report turbulence intensities between 30 and 45 percent at an equivalent downstream location from the injectors. The slightly higher intensities reported here are attributed to somewhat noisy LDA measurements rather than to a more turbulent flow structure.

For three injectors, the turbulence intensity peaked near the duct centerline where the concentration of jet fluid was highest. The turbulence intensity was relatively low near the circumference of the duct, confirming the earlier observation that this portion of the duct was relatively undisturbed by the crossflow injection.

LDA data taken at axial locations farther downstream from the injection points showed the same trends in velocity and turbulence intensity profiles. However, the magnitude in the variations decreased with distance. The flow once again took on profiles associated with fully developed flow, with the jet fluid dispersed throughout the free-stream cross-section. Classical duct-flow turbulence became the dominant flow structure in as little as one duct radius downstream from the crossflow injectors, although complete dispersion of the jet fluid required greater axial distances.

Standard Deviation of Mass Fraction - Using standard statistical techniques, the standard deviation of mass fraction from the well-mixed value was calculated from the tracer gas extractions at each axial test location. This calculation provided a measure of how well the flows were mixed at each axial test location. A deviation of zero would indicate completely well-mixed flows.

Figure II.H-8 illustrates the effect of jet diameter on mixing. The flow cases plotted had equal momentum ratios but differently sized injectors. All of the flow cases plotted employed 3 injectors, and the jets had sufficient momentum to penetrate to at least the center of the duct. The data show a trend toward better mixing as jet diameter is decreased, indicating that a smaller jet is more easily dispersed over the free-stream cross-section. Larger jets tend to stay more grouped together than smaller jets, all other conditions being equal.

Standard deviation data illustrating the effect of the number of injectors is plotted in Figure II.H-9. The total volumetric jet flowrate was equal in each of the cases plotted, and the number of injectors ranged from 1 to 4. All of the cases shown had sufficient energy for the injected fluid to impinge on either the opposing wall or an opposing jet plume. The data variation in this case is very small, indicating that the number of injectors is relatively unimportant, providing that the jets have sufficient energy to impinge on a wall or another jet plume. At lower jet momentum ratios, increasing the number of jets provides increased dispersion of jet fluid over the free-stream cross-section.

In summary, the mixing of a jet in crossflow was affected by the flow parameters investigated in this study in the following ways: First, free-stream Reynolds number was found to be relatively insignificant to jet mixing patterns providing that the flow was in the transitional or turbulent range. For laminar flow cases, density gradients can play an important role in jet behavior. Second, jet-to-main-flow momentum ratio was found to be the most important variable affecting jet trajectory and dispersion. At high momentum ratios the jet has more energy relative to the free stream, and can penetrate deeper into the main flow. Third, jet diameter was found to influence both jet trajectory and mixing rate. Since orifice size affects the momentum ratio for a given flowrate, jet diameter is important in its influence on momentum ratio. Also, mixing rate increases as jet diameter decreases, since a smaller jet is more easily dispersed into the free stream. And fourth, the number of crossflow injectors was found to be relatively unimportant, providing that the individual jet momentum ratios are high. For jets with low momentum ratios, increasing the number of jets provides greater dispersion of jet fluid over the free-stream cross-section.

Conclusions - An analysis of the data obtained in this study has shown that: 1) The trajectory of a round jet injected into a crossflow is a function of jet diameter, and the jet-to-free-stream momentum ratio; 2) Confining surfaces affect the jet trajectory only when the jet has sufficient energy to impinge on the opposing wall; 3) Mixing of free stream and crossflow jet fluid increases with distance downstream from the injection point, as the flows blend through turbulent diffusion. Far downstream from the injection ports, the flow is dominated by pipe-flow turbulence; 4) Mixing of a jet injected into a confined crossflow is enhanced when the jet has sufficient momentum to impinge

on another jet, or on a confining surface; 5) Buoyancy has a strong influence on crossflow jet behavior at free-stream Reynolds numbers typical of laminar flow. At higher Reynolds numbers, buoyancy effects are small; 6) The number of crossflow injectors used is relatively unimportant providing that the jet momentum is sufficient to cause the jet(s) to impinge on a solid surface or another jet. If jet momentum is not this high, increasing the number of injectors provides greater dispersion of the jet fluid over the free-stream cross-section; 7) Momentum ratio is the variable which most affects the penetration and mixing of crossflow jets; 8) Jet diameter influences both jet trajectory and mixing. The trajectory influence is primarily associated with the effect of jet diameter on the momentum ratio for a given flowrate. Smaller jets tend to be more easily dispersed into the free-stream fluid than larger jets; 9) The areas of highest axial velocity downstream from the lateral injection ports are associated with fluid from the free stream, which accelerates around the obstruction caused by the crossflow; 10) Turbulence intensity is highest in regions where crossflow jet fluid becomes entrained in the free stream.

Component 2 - Laboratory-Scale Reactor Modifications

This subtask component is aimed at making the modifications necessary in the BYU entrained-flow gasifier to conduct the sorbent injection tests carried out under Component 3. These modifications included incorporating sorbent injection ports and sight windows in the reactor shell. A sorbent feeder was also designed and constructed. Most of the modifications were discussed in the 7th Quarterly Progress Report.

Facility Modifications - To carry out the objective of this subtask, several facility modifications were made and additional equipment was designed and built. All modifications to the facility were completed during the last reporting period. Figure II.H-10 is a cross-section of the BYU gasifier. This figure shows the reactor section which was fabricated with two sight windows, spaced 180 degrees apart, to permit the use of an FTIR spectrometer. Also shown in this figure is the modified reactor section for the injection of sorbent. Three injection ports were spaced evenly around the outer diameter of the section. This set-up allows for one or three injection ports to be used. A pressurized rotary plate sorbent feeder (shown in Figure II.H-11) was designed and built. Using the feeder and injector ports, sorbent was injected independently from the coal feed system and at a lower temperature zone in the reaction chamber. A flash drum was also designed, built, and integrated into the scrubber system to prevent gases entrained in the quench water from being carried into the sewer.

At the beginning and throughout the testing period, the facility required a significant level of maintenance to keep it operational. This involved replacing gaskets, thermocouples, tubing and fittings in addition to recasting of the entire refractory liner.

Component 3 - Space-Resolved Sulfur and Nitrogen Pollutant Measurements

This subtask is aimed at determining the effect of sulfur sorbent ($CaCO_3$) on the concentration of sulfur pollutants in the BYU entrained-flow coal gasifier. The test plan called for sorbent to be both injected into the middle

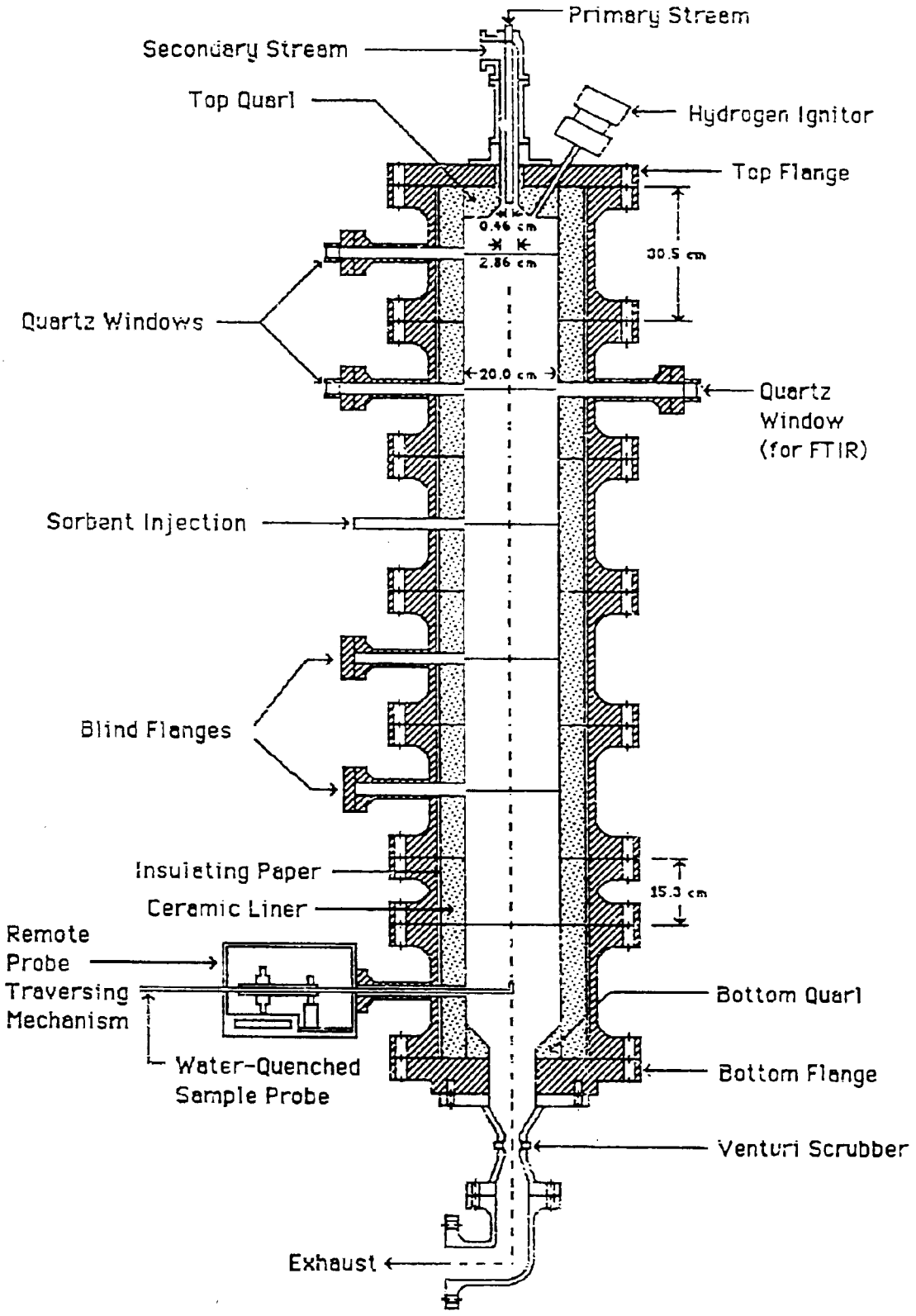

Figure II.H-10. Gasifier modified for sorbent injection and FTIR installation.

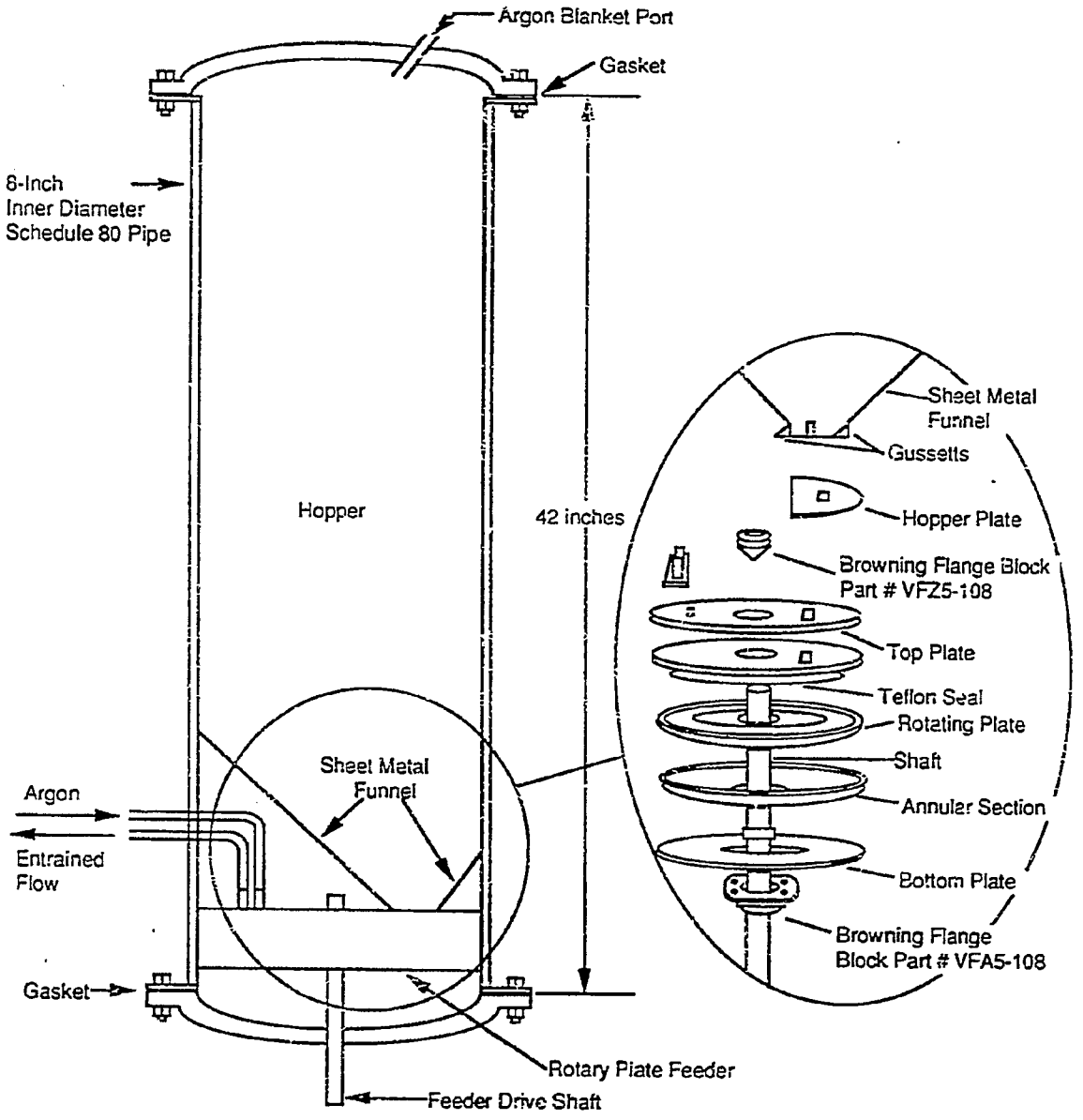

Figure II.H-11. Pressurized rotary plate sorbent feeder and hopper.

of the reaction section of the gasifier and fed with the coal as O_2/coal ratios and reactor pressures were varied for each of the test coals.

Test Program - Approximately one metric ton each of Utah bituminous, Illinois No. 6 bituminous, Pocahontas No. 3 bituminous, and Alberta subbituminous coal was obtained and pulverized. These coals have a wide range in their sulfur contents with weight percents of 0.45, 3.6, 0.64, and 0.07, respectively. As a source of sorbent, limestone containing 93.3% calcium carbonate ($CaCO_3$) was obtained and pulverized to about 6 microns (mass mean diameter).

Many checkout and calibration tests were conducted during the last quarter of the second year of the study to work out problems with the facility and sample system. Once the facility was operational, tests with the Alberta subbituminous coal were conducted with the assistance of Gary Kovacik, a visiting scientist from the Alberta Research Council in Canada.

At the conclusion of the Alberta test coals, Robert Carangelo of AFR brought an FTIR spectrometer to BYU and installed it on the gasifier. The new reactor section with the sight glasses provided optical access (See Fig. II.H-10). Tests were then conducted with both the Utah and Alberta coals to obtain FTIR spectral data, including the gas and particle temperatures along the line of sight through the reactor at the specified axial location. In the past, it has not been possible to obtain reliable internal temperatures in the gasifier. Knowledge of gas and particle temperatures is important for evaluating the comprehensive code and pollutant submodel being developed under Subtasks 3.a and 2.f, respectively, and in understanding what is occurring in the gasifier. The spectral data are being analyzed by AFR.

Table II.H-1 contains a summary of the tests that have been completed or are presently being conducted. Most of the planned tests have been completed. Tests with and without sorbent have been completed for the Utah, Alberta, Pocahontas and Illinois coals, and the mapping tests with the Utah coal are currently being conducted. As these tests are completed, the gas and liquid samples are analyzed to provide immediate feedback of what is occurring during the test run. The gas and liquid analysis results are being combined with the solids analysis results to provide required data. It will require the remainder of this calendar year to complete all of the remaining chemical analyses, to evaluate all of the data, and to determine what effect the presence of the sorbent had on the formation of the sulfur pollutant species.

Plans

Analysis of the data for the sorbent mixing fluid mechanics will continue, and a few additional tests may be considered. Maintenance of the gasifier facility will continue. The few remaining gasifier tests will be completed during the next month, and analysis of the test results will continue. Essentially all work on this subtask is expected to be completed during the next quarter.

Table II.H-1 Summary of Conducted Tests with the BYU Entrained Flow Gasifier.

Utah Bituminous Coal			
Test	Conditions	Sorbent	Purpose
1-7	0.8 O2/Coal, 1 atm pressure	No sorbent used	Checkout tests
8-10	0.8 O2/Coal, 5 atm pressure	No sorbent used	Checkout tests
11	0.5-0.9 O2/Coal, 1 atm pressure	No sorbent used	FTIR tests
12	0.75, 0.9 O2/Coal, 2 atm pressure	Sorbent fed with coal	Test plan
13	0.75, 0.9 O2/Coal, 4 atm pressure	Sorbent fed with coal	Test plan
14	0.75, 0.9 O2/Coal, 2 atm pressure	Sorbent injected (Hi rate)	Test plan
15	0.75, 0.9 O2/Coal, 4 atm pressure	Sorbent injected (Hi rate)	Test plan
16*	0.75, 0.9 O2/Coal, 2 atm pressure	Sorbent injected (Lo rate)	Test plan
17*	0.75, 0.9 O2/Coal, 4 atm pressure	Sorbent injected (Lo rate)	Test plan
18*	0.75 O2/Coal, 2 atm pressure	Sorbent injected	Mapping
Alberta Subbituminous Coal			
Test	Conditions	Sorbent	Purpose
1	0.7 O2/Coal, 1 atm pressure	No sorbent used	Checkout test
2	0.5-0.9 O2/Coal, 1 atm pressure	No sorbent used	FTIR tests
3	0.5-0.9 O2/Coal, 2 atm pressure	No sorbent used	Test plan
4	0.5-0.9 O2/Coal, 2 atm pressure	Sorbent fed with coal	Test plan
Pocahontas #3 Bituminous Coal			
Test	Conditions	Sorbent	Purpose
1	0.7 O2/Coal, 1 atm pressure	Sorbent fed with coal	Checkout test
2	0.75, 0.9 O2/Coal, 2 atm pressure	Sorbent fed with coal	Test plan
3	0.75, 0.9 O2/Coal, 2 atm pressure	Sorbent injected	Test plan
4	0.75, 0.9 O2/Coal, 4 atm pressure	Sorbent injected	Test plan
Illinois #6 Bituminous Coal			
Test	Conditions	Sorbent	Purpose
1-3	0.7 O2/Coal, 1 atm pressure	No sorbent used	Checkout tests
4	0.75, 0.9 O2/Coal, 2 atm pressure	Sorbent fed with coal	Test plan
5	0.75, 0.9 O2/Coal, 2 atm pressure	Sorbent injected	Test plan
6	0.75, 0.9 O2/Coal, 4 atm pressure	Sorbent injected	Test plan

* In process of conduction of these tests.